The Astrophysical Journal, 715:362–384, 2010 May 20 doi:10.1088/0004-637X/715/1/362
© 2010. The American Astronomical Society. All rights reserved. Printed in the U.S.A.

FLARING BEHAVIOR OF THE QUASAR 3C 454.3 ACROSS THE ELECTROMAGNETIC SPECTRUM

Svetlana G. Jorstad[1,2], Alan P. Marscher[1], Valeri M. Larionov[2,3], Iván Agudo[4], Paul S. Smith[5], Mark Gurwell[6], Anne Lähteenmäki[7], Merja Tornikoski[7], Alex Markowitz[8], Arkadi A. Arkharov[9], Dmitry A. Blinov[2], Ritaban Chatterjee[1], Francesca D. D'Arcangelo[1], Abe D. Falcone[10], José L. Gómez[4], Vladimir A. Hagen-Thorn[2,3], Brendan Jordan[11], Givi N. Kimeridze[12], Tatiana S. Konstantinova[2], Evgenia N. Kopatskaya[2], Omar Kurtanidze[12], Elena G. Larionova[2], Liudmilla V. Larionova[2], Ian M. McHardy[13], Daria A. Melnichuk[2], Mar Roca-Sogorb[4], Gary D. Schmidt[5], Brian Skiff[14], Brian Taylor[1,14], Clemens Thum[15], Ivan S. Troitsky[2], and Helmut Wiesemeyer[16]
[1] Institute for Astrophysical Research, Boston University, 725 Commonwealth Avenue, Boston, MA 02215, USA; jorstad@bu.edu
[2] Astronomical Institute, St. Petersburg State University, Universitetskij Pr. 28, Petrodvorets, 198504 St. Petersburg, Russia
[3] Isaac Newton Institute of Chile, St. Petersburg Branch, St. Petersburg, Russia
[4] Instituto de Astrofísica de Andalucía, CSIC, Apartado 3004, 18080, Granada, Spain
[5] Steward Observatory, University of Arizona, Tucson, AZ 85721-0065, USA
[6] Harvard-Smithsonian Center for Astrophysics, 60 Garden St., Cambridge, MA 02138, USA
[7] Metsähovi Radio Observatory, Helsinki University of Technology TKK, Metsähovintie 114, FIN-02540 Kylmälä, Finland
[8] Center for Astrophysics and Space Sciences, University of California, San Diego, M.C. 0424, La Jolla, CA 92093-0424, USA
[9] Main (Pulkovo) Astronomical Observatory of RAS, Pulkovskoye shosse, 60, 196140, St. Petersburg, Russia
[10] Deptartment of Astronomy & Astrophysics, Pennsylvania State University, 525 Davey Lab, University Park, PA 16802, USA
[11] School of Cosmic Physics, Dublin Institute of Advances Studies, Republic of Ireland
[12] Abastumani Astrophysical Observatory, Mt. Kanobili, Abastumani, Georgia
[13] Department of Physics and Astronomy, University of Southampton, Southampton, SO17 1BJ, UK
[14] Lowell Observatory, Flagstaff, AZ 86001, USA
[15] Institut de Radio Astronomie Millimétrique, 300 Rue de la Piscine, 38406 St. Martin d'Hères, France
[16] Instituto de Radio Astronomía Milimétrica, Avenida Divina Pastora, 7, Local 20, E-18012 Granada, Spain
Received 2009 November 16; accepted 2010 April 1; published 2010 April 28

ABSTRACT

We analyze the behavior of the parsec-scale jet of the quasar 3C 454.3 during pronounced flaring in 2005–2008. Three major disturbances propagated down the jet along different trajectories with Lorentz factors $\Gamma > 10$. The disturbances show a clear connection with millimeter-wave outbursts, in 2005 May/June, 2007 July, and 2007 December. High-amplitude optical events in the *R*-band light curve precede peaks of the millimeter-wave outbursts by 15–50 days. Each optical outburst is accompanied by an increase in X-ray activity. We associate the optical outbursts with propagation of the superluminal knots and derive the location of sites of energy dissipation in the form of radiation. The most prominent and long lasting of these, in 2005 May, occurred closer to the black hole, while the outbursts with a shorter duration in 2005 autumn and in 2007 might be connected with the passage of a disturbance through the millimeter-wave core of the jet. The optical outbursts, which coincide with the passage of superluminal radio knots through the core, are accompanied by systematic rotation of the position angle of optical linear polarization. Such rotation appears to be a common feature during the early stages of flares in blazars. We find correlations between optical variations and those at X-ray and γ-ray energies. We conclude that the emergence of a superluminal knot from the core yields a series of optical and high-energy outbursts, and that the millimeter-wave core lies at the end of the jet's acceleration and collimation zone. We infer that the X-ray emission is produced via inverse Compton scattering by relativistic electrons of photons both from within the jet (synchrotron self-Compton) and external to the jet (external Compton, or EC); which one dominates depends on the physical parameters of the jet. A broken power-law model of the γ-ray spectrum reflects a steepening of the synchrotron emission spectrum from near-IR to soft UV wavelengths. We propose that the γ-ray emission is dominated by the EC mechanism, with the sheath of the jet supplying seed photons for γ-ray events that occur near the millimeter-wave core.

Key words: galaxies: active – galaxies: jets – polarization – quasars: individual (3C 454.3) – X-rays: galaxies

1. INTRODUCTION

During the past four years, the quasar 3C 454.3 ($z = 0.859$) has displayed pronounced variability at all wavelengths. In spring 2005, it returned to the night sky with unprecedented brightness, $R \sim 12.0$ mag, a level not seen at optical wavelengths over at least 50 years of observations (Villata et al. 2006). An increase in activity occurred at X-ray and radio wavelengths as well, with the 230 GHz radio variations having a delay of ~2 months with respect to the optical variability (Raiteri et al. 2008a). This prominent outburst was followed by a more quiescent period at all wavebands from spring 2006 to spring 2007. During this interval, the optical spectrum possessed characteristics typical of radio-quiet active galactic nuclei (AGNs), such as a "big blue bump" and "little blue bump," attributed to thermal emission from the accretion disk and broad emission lines from surrounding clouds, respectively (Raiteri et al. 2007). After the quiescent state, the quasar underwent a new stage of high optical activity (Raiteri et al. 2008b) that continued to the end of 2008. During this time span, very bright γ-ray emission was detected (Vercellone et al. 2008; Tosti et al. 2008), with an excellent correlation between the γ-ray and near-infrared/optical variations (Bonning et al. 2009).

Models proposed to explain the observed variability and spectral energy distribution (SED) of 3C 454.3 across the electromagnetic spectrum involve processes originating in the radio jet of the quasar. Villata et al. (2007) suggest that the very high optical flux in spring 2005 was connected with a

disturbance (e.g., a shock) propagating along a curved trajectory in the jet, with optical synchrotron photons emitted over a different volume than the longer-wavelength radiation. As the emission zone of a given wavelength passes closest to the line of sight, the flux peaks at that wavelength. This occurs first at optical and later at longer wavelengths. Ghisellini et al. (2007) have found that the behavior of 3C 454.3 in 2005–2007 is consistent with the model suggested by Katarzynski & Ghisellini (2007), in which the dissipation site of an outburst depends on the bulk Lorentz factor and compactness of the perturbation propagating down the jet. Outbursts occurring closer to the black hole (BH) should have a more compact emitting region with a lower bulk Lorentz factor, Γ, and a stronger magnetic field, B. Greater compactness of the emission region intensifies the synchrotron flux as well as the high-energy component produced via the synchrotron self-Compton (SSC) mechanism, while the external Compton (EC) high-energy component (inverse Compton radiation with seed photons from outside the jet) is suppressed owing to a weaker Doppler factor, δ, resulting from the lower value of Γ. Ghisellini et al. (2007) model the outburst in 2005 as an event that occurred closer to the BH ($\Gamma \sim 8$, $\delta \sim 13$, $B \sim 15$ G, and size of the emitting region $a \sim 5.5 \times 10^{-3}$ pc) than the outburst in 2007 ($\Gamma \sim 16$, $\delta \sim 16$, $B \sim 9$ G, and $a \sim 8 \times 10^{-3}$ pc). Sikora et al. (2008) argue that the optical, X-ray, and millimeter light curves during the outburst in 2005 require a release of a significant fraction of the jet energy when the jet becomes transparent at millimeter wavelengths at the millimeter-wave "photosphere." These authors conclude that this photosphere is located at ~10 pc from the BH, coinciding with the expected location of a torus of hot dust. Sikora et al. (2008) infer that the X-ray and γ-ray emission is most likely produced via the EC mechanism, with seed photons emitted by the hot dust scattered by relativistic electrons in a plasma with bulk Lorentz factor $\Gamma \sim 20$. Interpretations of γ-ray observations with *AGILE* during autumn 2007 and the densely sampled light curve provided by the *Fermi Gamma-ray Space Telescope* starting in 2008 August, combined with simultaneous observations at longer wavelengths, involve higher-energy electrons that emit synchrotron radiation at near-IR and optical wavelengths as well as scatter external photons from the broad-line region to energies up to ~100 GeV (Vercellone et al. 2009; Bonning et al. 2009).

Jorstad et al. (2005) monitored the quasar 3C 454.3 at 43 GHz with the Very Long Baseline Array (VLBA) bimonthly from 1998 March to 2001 April, and determined parameters of the parsec-scale jet during this period based on the apparent speed of superluminal knots (also referred to as "components" of the jet) and timescale of their flux variability. They found that the jet of 3C 454.3 during this time span had physical parameters as follows: $\Gamma = 15.6 \pm 2.2$, $\Theta_\circ = 1\overset{\circ}{.}3 \pm 1\overset{\circ}{.}2$, $\delta = 24.6 \pm 4.5$, and $\theta = 0\overset{\circ}{.}8 \pm 0\overset{\circ}{.}2$, where $\Theta_\circ$ is the viewing angle and θ is the opening half-angle of the jet. The Boston University group resumed VLBA monitoring of the quasar in 2005 June, and has continued to monitor the source within a program of roughly monthly VLBA imaging of bright γ-ray blazars at 43 GHz. In this paper, we analyze disturbances seen in the quasar jet during the period of high optical activity in 2005–2008, and connect events in the jet with prominent variability at different wavebands. Observations cover the range of frequencies from 10^{10} GHz to 10^{23} GHz, which provide significantly different angular resolutions at which an event is observed—10–15 arcmin at high-energy frequencies, ~5 arcsec at millimeter and submillimeter wavelengths, ~1 arcsec in the optical and IR bands, and ~0.1 milliarcsecond (mas) with the VLBA at 43 GHz. This renders interpretation of multifrequency behavior challenging, and makes analysis of variability at different wavelengths along with VLBI images the main tool for understanding processes and mechanisms involved in the physics of blazars.

2. MULTIFREQUENCY LIGHT CURVES

We have analyzed light curves of the quasar 3C 454.3 from γ-ray to radio wavelengths during the period 2004–2009. We use relative Julian dates (RJD $\equiv$ JD $-$ 2450000) to refer to the epochs of observation.

2.1. Optical, Ultraviolet, and Near-infrared Photometric Data

We use the optical light curve in R band collected by the WEBT collaboration (Villata et al. 2006, 2007; Raiteri et al. 2008a, 2008b), which covers the period from 2003 December 28 to 2008 February 8 (RJD: 3001–4505). To this, we add the data from the 2 m robotic Liverpool telescope at the Observatorio del Roque de Los Muchachos (La Palma, Spain) and the 1.8 m Perkins telescope of Lowell Observatory (Flagstaff, AZ). We have extended the light curve up to 2009 January 7 (RJD: 4839) using the data obtained at the Perkins telescope, 70 cm telescope of the Crimean Astrophysical Observatory (Nauchnij, Ukraine), 40 cm telescope of St. Petersburg State University (St. Petersburg, Russia), 2.2 m telescope of the Calar Alto Observatory (Spain), and 70 cm telescope of Abastumani Observatory (Republic of Georgia). At some telescopes, the photometric data have been carried out not only in R band but also in B, V, and I filters, although less frequently than in R band. We use these data for broadband spectral analysis. The data from 2008 June 23 to December 10 (RJD: 4640–4810) are supplemented by measurements by the SMARTS consortium, posted at their Web site.[17]

We have performed the U-band (3500 Å) observations of the quasar with the Liverpool telescope from 2005 May 18 to December 10 (160 measurements) and reduced the data in a manner used in the WEBT collaboration (Raiteri et al. 2008b). We have obtained archived UVOT *Swift* data from 2005 April 24 to 2009 January 27 in four filters, U (3501 Å), $UW1$ (2634 Å), $UM2$ (2231 Å), and $UW2$ (2030 Å) (86, 100, 89, and 95 measurements, respectively). The UVOT data were reduced using the HEASOFT 6.5 package and following the threads provided by the UVOT User's Guide and recommendations contained in the release notes with parameters similar to those used by Raiteri et al. (2008b). We have adopted galactic extinction values derived by Raiteri et al. (2008b): 0.58 (U), 0.73 ($UW1$), 1.07 ($UM2$), and 1.02 mag ($UW2$).

We use infrared (IR) JHK data collected at the 1.1 m telescope of the Main (Pulkovo) Astronomical Observatory of the Russian Academy of Sciences located at Campo Imperatore, Italy (Larionov et al. 2008). The values of Galactic extinction provided by the *NASA Extragalactic Database* are adopted to correct the photometric estimates for Galactic absorption. We have applied the calibration of Mead et al. (1990) for all optical and IR measurements to transform magnitudes into flux densities. Figure 1 shows the optical light curve of the quasar in R band, the UV light curves in U and $UW1$ bands, and the near-IR light curve in K band from 2004 January to 2009 January.

[17] http://www.astro.yale.edu/smarts/glast/

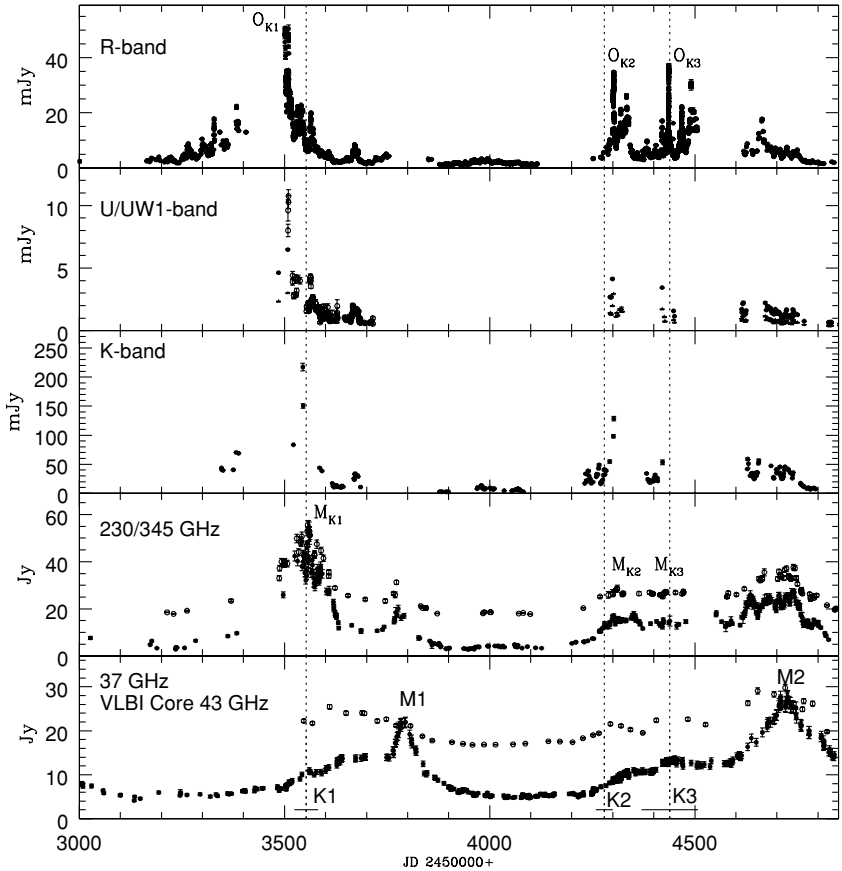

Figure 1. Light curves of the quasar 3C 454.3 at different frequencies. Dotted lines show times of ejections (times of coincidence with the position of the VLBI core at 43 GHz) of superluminal components $K1$, $K2$, and $K3$ and solid line segments show uncertainties in the ejection times; second panel: open circles—Liverpool telescope data in U band, open triangles—*Swift* UVOT data in U band, and filled triangles—*Swift* UVOT data in $UW1$ band; 345 GHz (open circles, fourth panel) and 43 GHz measurements (open circles, fifth panel) are shifted by +15 Jy for clarity. Symbols designate the most prominent outbursts at different wavelengths.

2.2. Radio Light Curves

The 230 GHz (1.3 mm) and 345 GHz (0.85 mm) light curves were obtained at the Submillimeter Array (SMA), Mauna Kea, Hawaii from 2004 June 16 to 2009 January 31 (RJD: 3172–4862). 3C 454.3 is a bright quasar included in an ongoing monitoring program at the SMA to determine the fluxes of compact extragalactic radio sources that can be used as calibrators at millimeter and submillimeter wavelengths. Data from this program are updated regularly and are available at SMA Web site.[18] Details of the observations and data reduction can be found in Gurwell et al. (2007).

The data at 230 GHz are supplemented by measurements carried out at the 30 m telescope of Instituto de Radio Astronomía Milimétrica (IRAM, Granada, Spain). The IRAM 30 m telescope observed simultaneously at 86.24 GHz (3.5 mm) and 228.93 GHz (1.3 mm) by making use of the A100/B100 and A230/B230 pairs of orthogonally linearly polarized heterodyne receivers, respectively. Every IRAM 30 m measurement was preceded by a cross-scan pointing of the telescope toward 3.5 mm and 1.3 mm calibration sources. Such measurements consisted of a series of wobbler-switching on–offs with total integration times of 4–8 minutes, depending on the total flux density of the source and atmospheric conditions. Measurements of Mars and/or Uranus were obtained at least once per observing session in order to estimate and subtract residual instrumental polarization, and to calibrate the absolute total flux density scale. Whenever these planets were not visible, the compact H II regions W3 OH, K3-50A, and NGC 7538, and/or the compact planetary nebula NGC 7027 were observed for calibration. The initial calibration of the amplitude was performed through the telescope's online data processing procedures within the MIRA-GILDAS software.[19] The remaining data reduction involved the removal of outliers, an elevation dependent calibration, and the calibration of the absolute flux density scale as described in Agudo et al. (2006). The final flux density error of every measurement also included an additional 5% non-systematic uncertainty added in quadrature. Finally, the resulting data were averaged for those observing epochs on which more than one measurement was obtained.

The 37 GHz (8 mm) observations were performed with the 13.7 m telescope at Metsähovi Radio Observatory of Helsinki University of Technology, Finland. The flux density calibration is based on observations of DR 21, with 3C 84 and 3C 274 used as secondary calibrators. A detailed description of the data reduction and analysis is given in Teräsranta et al. (1998). The radio light curves are plotted in Figure 1.

2.3. High-energy Light Curves

We obtained 63 measurements of 3C 454.3 with the *Rossi X-ray Timing Explorer* (*RXTE*) from 2005 May 11 to September 5 (RJD: 3502–3619). Each *RXTE* visit lasted ∼1 ks. We used data taken with *RXTE*'s Proportional Counter Array (PCA), which is

[18] http://sma1.sma.hawaii.edu/postobserving.html

[19] http://www.iram.fr/IRAMFR/GILDAS/doc/html/mira-html

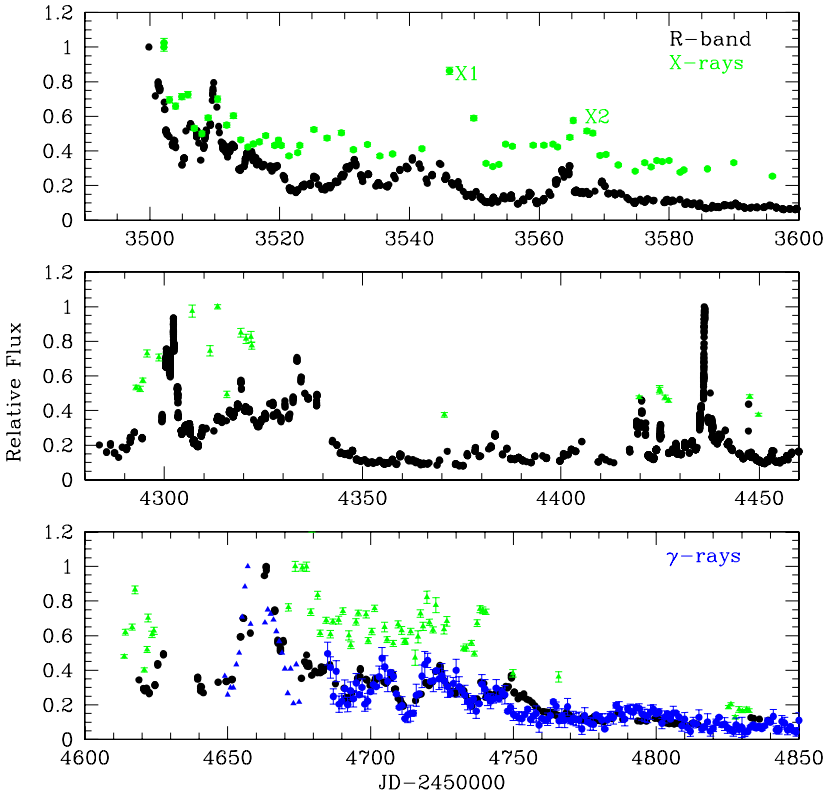

Figure 2. Normalized *R* band (black), X-ray (green, *RXTE* measurement—circles and *Swift* measurements—triangles), and γ-ray (blue) light curves for three periods. The maximum flux within each panel is adopted as the normalization factor. Top panel: $S_{\rm R}^{\rm max} = 63.6$ mJy, $S_{\rm X}^{\rm max} = 10.13$ μJy (X-ray flux is at 4 keV); middle panel: $S_{\rm R}^{\rm max} = 37.17$ mJy, $S_{\rm X}^{\rm max} = 2.138$ counts s^{-1} (X-ray flux is at 0.3–10 keV); bottom panel: $S_{\rm R}^{\rm max} = 17.82$ mJy, $S_{\rm X}^{\rm max} = 1.614$ counts s^{-1}, $S_{\gamma}^{\rm max} = 1.2 \times 10^{-5}$ photons cm^{-2} s^{-1} (X-ray flux is at 0.3–10 keV, γ-ray flux is at 0.1–300 GeV). Blue triangles show the γ-ray measurements taken from Figure 1 of Abdo et al. (2009b). Error bars for the optical observations are less than the size of symbols.

collimated to have an FWHM 1° field of view. However, there is a cataclysmic variable star, IM Peg, located about 0.°72 to the NW of 3C 454.3 (Perryman et al. 1997). To completely eliminate contributions to the observed spectrum of 3C 454.3 from IM Peg, we chose an *RXTE* on-axis pointing position 0.°52 to the SE of 3C 454.3; at this offset position, the PCA collimator efficiency is 45% (Jahoda et al. 2006); we corrected for this when generating the PCA response matrices (see below). Reduction of the PCA data followed standard extraction and screening procedures, using HEASOFT version 6.0 software.[20] PCA STANDARD-2 data were collected from Proportional Counter Unit (PCU) 2 only. We use the "L7-240" background models, appropriate for faint sources. Response matrices were generated for each spectrum separately using the FTOOLS program PCARSP. We modeled the 3–15 keV spectrum in XSPEC v.11 with a single power-law and Galactic absorption corresponding to a hydrogen column density $N_{\rm H} = 7.2 \times 10^{20}$ cm^{-2} (Elvis et al. 1989), and calculated the light curve of X-ray flux density at 4 keV.

For the period from 2005 May 10 to 2009 January 27 (RJD: 3501–4858), we used publicly available data from the *Swift* satellite[21] that were carried out with the X-Ray Telescope (XRT) at 0.3–10 keV (95 measurements) and processed through the XRT pipeline. We checked the data: the PC mode to WT mode transitions are well handled, the rates are self-consistent, implying that there are no problems with the point-spread-function correction factors; the uncertainties are $\lesssim$2%.

We obtained Photon and Spacecraft data from the Fermi Science Support Center (FSSC) for observations with the Large Area Telescope (LAT) from 2008 August 5 to 2009 February 10 (RJD: 4684–4873) within a 15° radius centered on the quasar. We then calculated the γ-ray light curve of 3C 454.3 at 0.1–300 GeV with daily binning using the software and following the Analysis Threads provided by the FSSC. The procedure included selection of good data and time (programs: *gtselect, gtmktime*), construction of the exposure map for each day (*gtltcube, gtexpmap*), and modeling of the data by a single power law, optimized via a maximum-likelihood method (*gtlike*). We used the response function generated by the FSSC, and created a model file that consisted of a power-law model (prefactor and index) for 3C 454.3 and three other bright γ-ray sources in the field: PKS 2201+171, CTA102, and PKS 2325+093 (Abdo et al. 2009a), and diffuse emission models for Galactic and extragalactic background provided by the FSSC. We consider the quasar to be detected if the test statistic, TS, calculated by the *gtlike* procedure exceeds 10, corresponding to at least a 3σ detection level (Abdo et al. 2009a). For such measurements, we derived γ-ray flux estimates with uncertainties within 10%–15%. We have supplemented these γ-ray data by the measurements from RJD: 4649–4675 taken from Figure 1 of Abdo et al. (2009b), which are not provided by the LAT Data Server. Figure 2 shows the high-energy light curves for three time intervals when the X-ray and γ-ray measurements were available along with the optical light curve.

3. POLARIZATION OBSERVATIONS

We have obtained linear polarization measurements of 3C 454.3 at optical and millimeter wavelengths. All of these data

[20] http://heasarc.gsfc.nasa.gov/ftools/
[21] http://www.swift.psu.edu/monitoring/

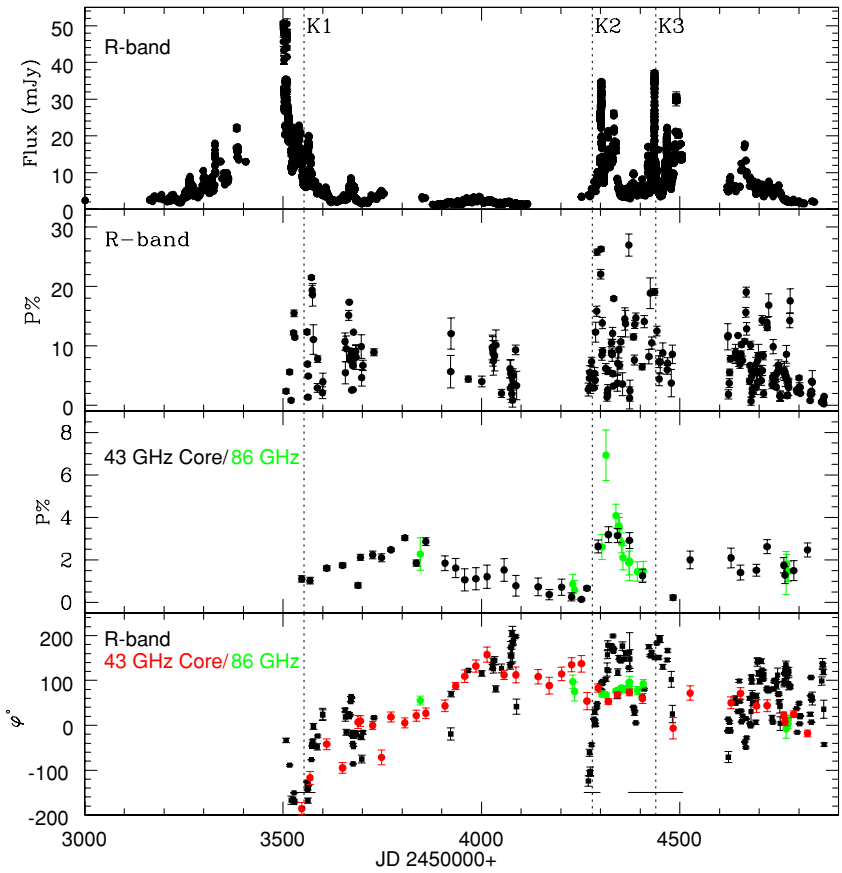

Figure 3. Flux and polarization curves of the quasar 3C 454.3 at different frequencies: —total flux density in *R* band; second panel—degree of polarization at optical wavelengths; third panel—degree of polarization at 86 GHz (green circles) and in the VLBI core at 43 GHz (black circles); and bottom panel—position angle of polarization at optical wavelengths (black circles), at 86 GHz (green circles), and in 43 GHz VLBI core (red circles); dotted lines show times of ejections of superluminal components and solid line segments show uncertainties in the ejection times. Values of $\varphi_{7\mathrm{mm}}$ are corrected for RM according to Jorstad et al. (2007).

were checked for consistency and corrected for statistical bias (Wardle & Kronberg 1974).

3.1. Optical Polarization Data

Our optical polarization monitoring in *R* band of γ-ray blazars, including 3C 454.3, began in 2005 May at the 70 cm telescope of the Crimean Astrophysical Observatory. The telescope is equipped with an ST-7 based photometer–polarimeter. The details of the observation and data reduction can be found in Larionov et al. (2008).

Since 2005 September, we have obtained polarimetric observations at the Perkins telescope of Lowell Observatory (Flagstaff, AZ) with the PRISM camera[22] supplemented by a polarimeter with a rotating half-waveplate. These involve a series of 5–7 Stokes *Q* and *U* measurements for a given object. Each series consists of four measurements at instrumental position angles (P.A.s) 0°, 45°, 90°, and 135° of the waveplate. Since the camera has a wide field of view ($14' \times 14'$), we use field stars to perform both interstellar and instrumental polarization corrections. We use unpolarized calibration stars from Schmidt et al. (1992) to check the instrumental polarization, which is usually within 0.3%–0.5%, and polarized stars from the same paper to calibrate the polarization P.A.

In 2006 November, the 40 cm telescope of St. Petersburg State University joined the program. The telescope is equipped with a nearly identical photometer–polarimeter as that of the 70 cm telescope in Crimea, and the observations and data reduction are carried out in the same manner (Larionov et al. 2008). However, the polarization observations are performed without a filter, with central wavelength $\lambda_{\mathrm{eff}} \sim 670$ nm.

Starting in 2007 July, the MAPCAT (Monitoring AGN with Polarimetry at the Calar Alto Telescopes)[23] program has made use of the CAFOS (Calar Alto Faint Object Spectrograph) in its imaging polarimetric mode on the 2.2 m telescope at the Calar Alto Observatory (Almería, Spain). Every *R*-band polarization measurement consisted of four imaging exposures of ∼50 s at 0°, 22.°5, 45°, and 67.°5 of the $\lambda/2$ plate in CAFOS. Polarization measurements of at least two polarized standard stars from Schmidt et al. (1992) were performed to estimate the instrumental polarization, which is ∼0.2%. The degree (p) and P.A. (φ) of linear polarization were obtained from their relation with the eight flux measurements, as described in Zapatero et al. (2005).

We have obtained polarization data at Steward Observatory with the 1.54 m Kuiper during a 2005 campaign from October 25 to November 4 (details given in D'Arcangelo et al. 2009), and within another, currently operating program at that telescope and the 2.3 m Bok Telescope to provide optical polarization measurements for bright γ-ray blazars from the *Fermi* LAT-monitored blazar list.[24] The combined optical polarization data are presented in Figure 3.

[22] http://www.bu.edu/prism/

[23] http://www.iaa.es/∼iagudo/research/MAPCAT/MAPCAT.html

[24] http://james.as.arizona.edu/∼psmith/Fermi

3.2. Millimeter-wave Polarization Data

The IRAM 30 m telescope also performed linear and circular polarization at 86.24 GHz. The A100/B100 pair of orthogonally linearly polarized heterodyne receivers is connected to the XPOL polarimeter (Thum et al. 2008), which provides 500 MHz bandwidth per receiver. We have carried out the initial calibration of the phase through the telescope's online data processing procedures within the MIRA-GILDAS software. The subsequent polarimetric data reduction follows that of Thum et al. (2008) and Agudo et al. (2010). These procedures involve the removal of outliers and of systematic residual instrumental polarization still present in the data, calibration of the absolute flux density scale, estimation of remaining non-systematic or statistical uncertainties still affecting the data, and quadratic addition of the latter to the final uncertainties of the measurements. Such final errors are ∼0.5 % in Stokes Q and U parameters, and ∼0.3 % in Stokes V parameter. The data are plotted in Figure 3.

4. VLBA OBSERVATIONS

We observed 3C 454.3 in the course of a program of monthly monitoring of bright γ-ray blazars with the VLBA at 43 GHz (7 mm).[25] During the period from 2005 June to 2009 May, we obtained 44 total and polarized intensity images of the quasar at a resolution of ∼0.3 × 0.1 mas. Figure 4 presents a sequence of total intensity images, with several images per year convolved with the same beam and with contours based on the same global map peak. We performed the data reduction in the manner of Jorstad et al. (2005) using the Astronomical Image Processing System (AIPS) and Difmap (Shepherd 1997). In addition to the standard resolution beam of uniform weighting of the uv-data, we have convolved the images with a beam of FWHM diameter of 0.1 mas comparable to the resolution of the longest baselines of the VLBA. Figure 5 shows the morphology of the parsec-scale jet of 3C 454.3, convolved with a standard beam along with an image with the smaller beam that features knots $K1$, $K2$, $K3$, and C found in the jet (see Section 5). Although the synthesized beam of the VLBA observations along the jet is ∼0.1 mas, we have convolved the core region of the jet with a circular beam with an FWHM diameter of 0.05 mas for epochs when all antennas were in operation and the weather was favorable. Since this is only 30% smaller than the FWHM angular resolution of the longest baseline, 0.07 mas, the array partially resolves structures on 0.05 mas scales. At the majority of suitable epochs, the resulting super-resolved map of the core region consists of three components, as shown in Figure 6. Such a structure is especially apparent when the core is not disturbed by passage of a moving knot (bottom panel). To support the conclusion that this fine structure in the core is real, we have constructed similar super-resolved images of the quasar CTA102, obtained with the VLBA along with 3C 454.3. Since CTA102 is close to 3C 454.3 in the sky, the observations have similar uv-coverage. The resulting images of CTA102 contain only single-component cores. This suggests that the fine structure of the core of 3C 454.3 is not an artifact of the smaller beam.

Since VLBA data yield only the relative orientation of the electric vector P.A. (EVPA) across a source, special attention was paid to the calibration of the absolute EVPA values. We employed data from the NRAO VLA/VLBA Polarization

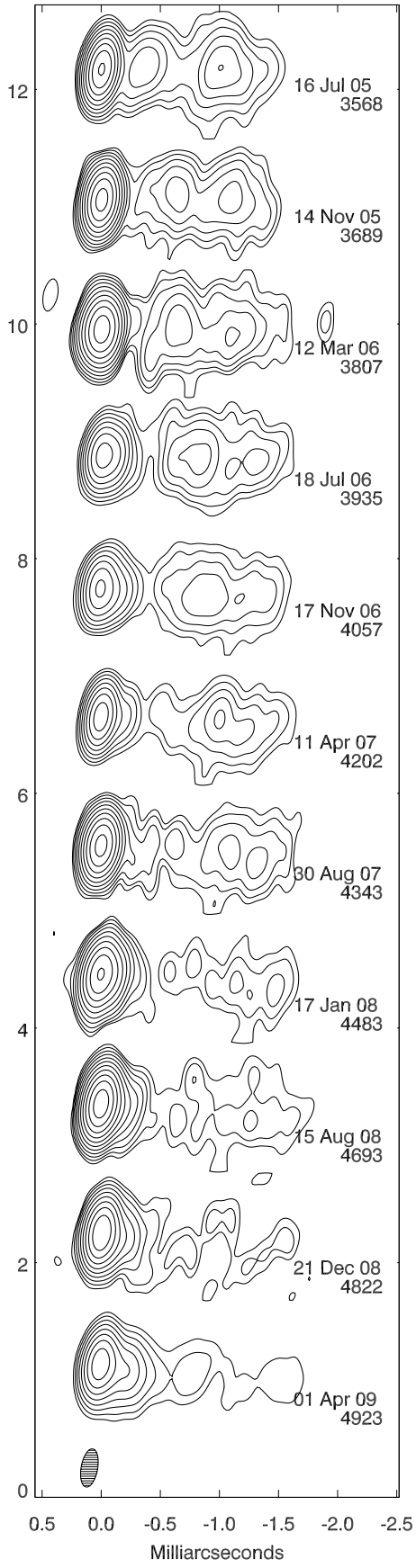

Figure 4. 43 GHz total intensity images of the quasar 3C 454.3 with $S_{\rm peak}$ = 19.43 Jy beam^{-1} and beam = 0.14 × 0.30 mas^2 at P.A. = −10°. Contours represent 0.0625%, 0.125%, 0.25%,... 64% intensity of the peak.

[25] http://www.bu.edu/blazars/VLBAproject.html

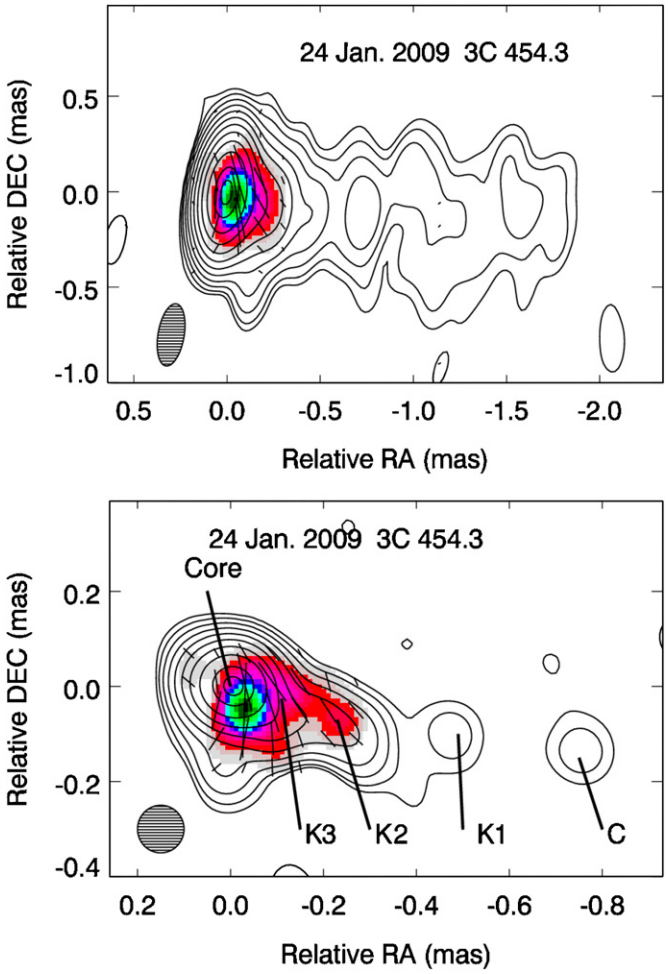

Figure 5. 43 GHz total (contours) and linearly polarized (color scale) intensity images of 3C 454.3 with different convolving beams; top: 0.33 × 0.14 mas^2 at P.A. = −10°, $S_{\rm peak}$ = 6.20 Jy, $S^{\rm p}_{\rm peak}$ = 0.076 Jy; bottom: 0.10 × 0.10 mas^2, $S_{\rm peak}$ = 5.66 Jy, $S^{\rm p}_{\rm peak}$ = 0.067 Jy. Line segments show the plane of polarization and letters identify components in the jet.

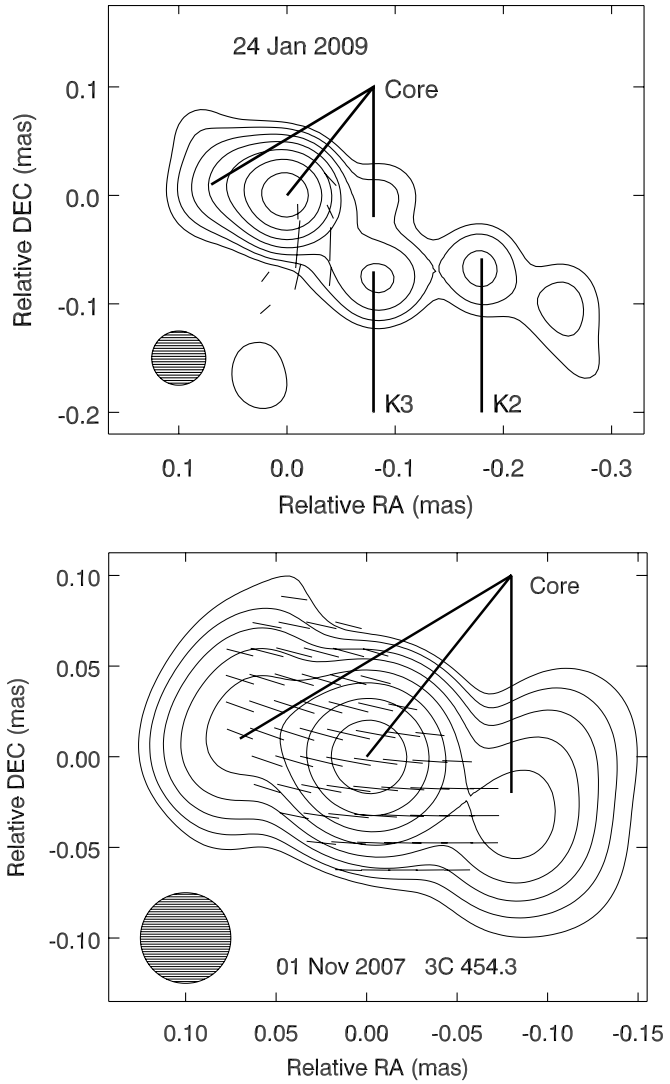

Figure 6. 43 GHz total (contours) intensity images of 3C 454.3 with convolving beam 0.05 × 0.05 mas^2 at different epochs; top: 2009 January 24 (RJD: 4856) $S_{\rm peak}$ = 5.10 Jy, $S^{\rm p}_{\rm peak}$ = 0.067 Jy; bottom: 2007 November 1 (RJD:4406) $S_{\rm peak}$ = 5.84 Jy, $S^{\rm p}_{\rm peak}$ = 0.050 Jy. Line segments show the plane of polarization and letters identify components in the jet. The tripod of lines indicates a three-component structure of the core.

Calibration Page,[26] which provides EVPA measurements with the VLA at 43 GHz, integrated over the entire source for several objects from our sample observed with the VLBA (OJ287, 1156+295, 3C 273, 3C 279, BL Lac, and 3C 454.3). For other epochs without contemporaneous VLA observations, we used the *D-terms* method described by Gómez et al. (2002). The accuracy of the absolute EVPA calibration is within 4°–8°. Jorstad et al. (2007) provide an estimate of the Faraday rotation measure (RM) of $(-6.8 \pm 3.7) \times 10^3$ rad m^{-2} in the millimeter-VLBI core of 3C 454.3, corresponding to a correction for the EVPA at 43 GHz of $-19° \pm 10°$. Although the estimate of RM has a large uncertainty and is not simultaneous with the VLBA observations reported in this paper, we find that applying the RM correction at 43 GHz improves the similarity between the behavior of EVPAs at 86 GHz and 43 GHz. Figure 3 shows the results of our measurements of degree (p_{43}) and P.A. (φ_{43}) of polarization in the core region of the quasar.

4.1. Modeling of Images

We have modeled our calibrated uv-data with point source brightness distributions using the *Difmap* task MODELFIT. The number of point-like components required to fit the data was determined by the best agreement between the model and data according to χ^2 values, with reduced χ^2 ranging from 1.0 to 5. Since we have roughly monthly observations with the VLBA, the model yielding the best agreement at a given epoch was used as an input model for the following epoch in order to maximize consistency across epochs given the complexity of the brightness distribution. We then performed 100 iterations to adjust the input model to the uv-data of the second epoch, editing the model if deleting or adding components was required to represent the image. We assumed that the core is a stationary component at relative right ascension and declination (0,0), and then determined for each component the total and polarized flux intensity, S_{43} and $S^{\rm p}_{43}$, respectively, distance from the core, R, P.A. relative to the core, Θ, degree of polarization, p_{43}, and P.A. of polarization, φ_{43}. We have identified components across the epochs in the manner described in Jorstad et al. (2005) and used their method, as well as the same cosmological parameters ($\Omega_{\rm m}$ = 0.3, Ω_Λ = 0.7, and $H_\circ$ = 70 km s^{-1} Mpc^{-1}), to

[26] http://www.vla.nrao.edu/astro/calib/polar/

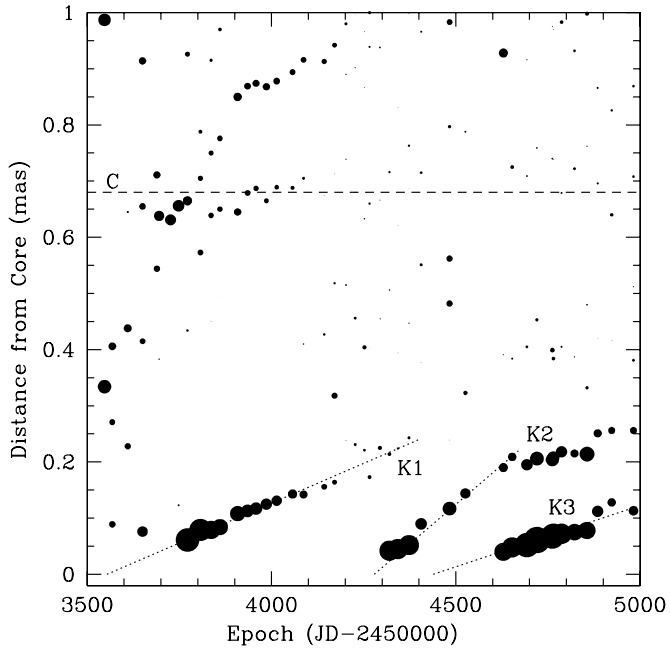

Figure 7. Distance of components from the 43 GHz core as a function of time. The size of each symbol is proportional to the logarithm of the flux density of the knot. Dotted lines indicate an approximation for the presumably ballistic motion of components $K1$, $K2$, and $K3$ near the core. The dashed line shows the position of stationary knot C reported by Jorstad et al. (2005).

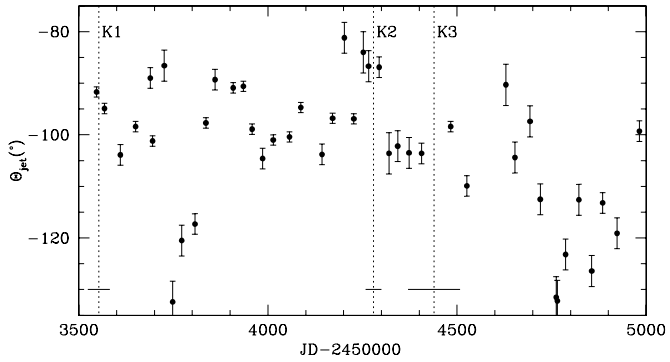

Figure 8. Direction of the jet within 0.3 mas from the core as a function of time. Dotted lines show the times of ejections of superluminal components $K1$, $K2$, and $K3$ from the 43 GHz core and solid line segments show uncertainties in the ejection times.

calculate the proper motions and apparent speeds of moving features. Figure 1 shows the light curve of the VLBI core, while Figure 7 presents the positions of all components (except the core) brighter than 50 mJy found within 1 mas of the core during the period 2005 June to 2009 May (RJD: 3547–4982).

Our analysis of the VLBA images concentrates on the innermost region of the jet. Figure 8 shows the projected jet direction, $\Theta_{\rm jet}$, determined at each epoch according to the P.A. of the brightest component within 0.1–0.3 mas of the core. The average jet direction is $\langle\Theta_{\rm jet}\rangle = -95^\circ \pm 8^\circ$. Figure 8 shows that there are significant deviations of $\Theta_{\rm jet}$ from the average, which might reflect intrinsic changes of the jet direction or shifts in the brightness distribution across the width of the jet.

5. DISTURBANCES IN THE INNER JET

Analysis of the images reveals three features moving with respect to the core for which the apparent speed, $\beta_{\rm app}$, and time of ejection (coincidence with the core), $T_\circ$, can be estimated.

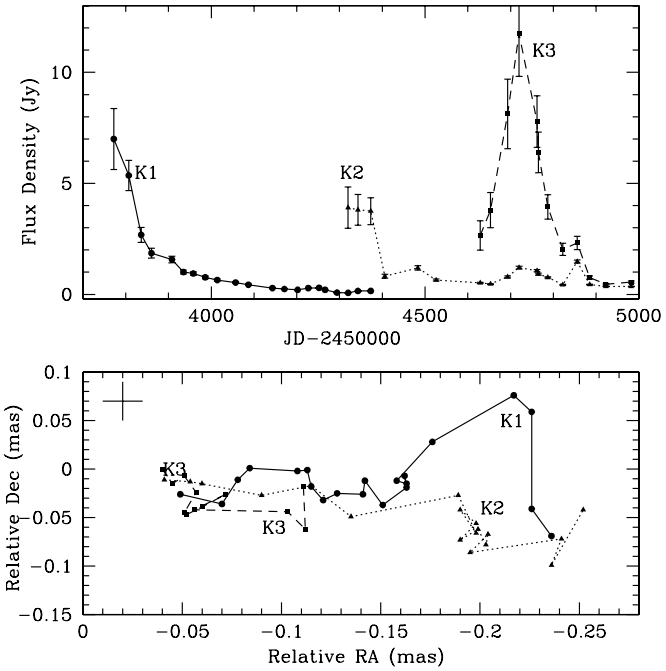

Figure 9. Light curves (top) and trajectories (bottom) of moving knots; the cross indicates typical uncertainties in position of components (upper left corner of the bottom panel).

We have designated the features as components $K1$, $K2$, and $K3$ (Figure 7). The majority of images show a brightness enhancement at 0.6–0.7 mas from the core, which is most likely associated with component C reported by Jorstad et al. (2005) as a stationary knot at position $R \sim 0.63$ mas. Knots $K1$ and $K2$ move ballistically only within 0.2 mas of the core. Beyond 0.2 mas, $K1$ accelerates and fades, while $K2$ decelerates and brightens. Figure 9 shows light curves and trajectories of components. Although the separation of $K3$ from the core is at the limit of our resolution, modeling requires the presence of two components in the core region at all epochs starting from 2008 June, with a persistent increase in separation between the components at later epochs. Figures 10, 11, and 12 show sequences of total and polarized intensity images displaying the jet evolution that we attribute to the emergence of components $K1$, $K2$, and $K3$, respectively. Knots $K1$ and $K2$ are distinct on the high-resolution total intensity maps and have better alignment of the P.A. of the polarization with the jet direction than does the polarization of the core. The brightest knot, $K3$, fades dramatically while it is still very close to the core.

Since we are interested mainly in the time of ejection of the components and their speed in the vicinity of the core, we have used only those epochs when the components moved ballistically (the first 10 and 8 epochs for $K1$ and $K2$, respectively, and all 11 epochs for $K3$) for deriving kinematic parameters. The parameters and their uncertainties were obtained in the manner described in Jorstad et al. (2005).

We modeled components by point sources because such an approach gives better consistency between epochs than, for example, modeling by components with circular Gaussian brightness distributions. This suggests that the knots are very compact, with angular size smaller than half the beam axis along the jet, $\lesssim$0.07 mas. We have adopted an FWHM size of 0.05 mas for all three components to estimate Doppler and Lorentz factors and viewing angle independently by using the method developed for high-frequency VLBI monitoring (Jorstad

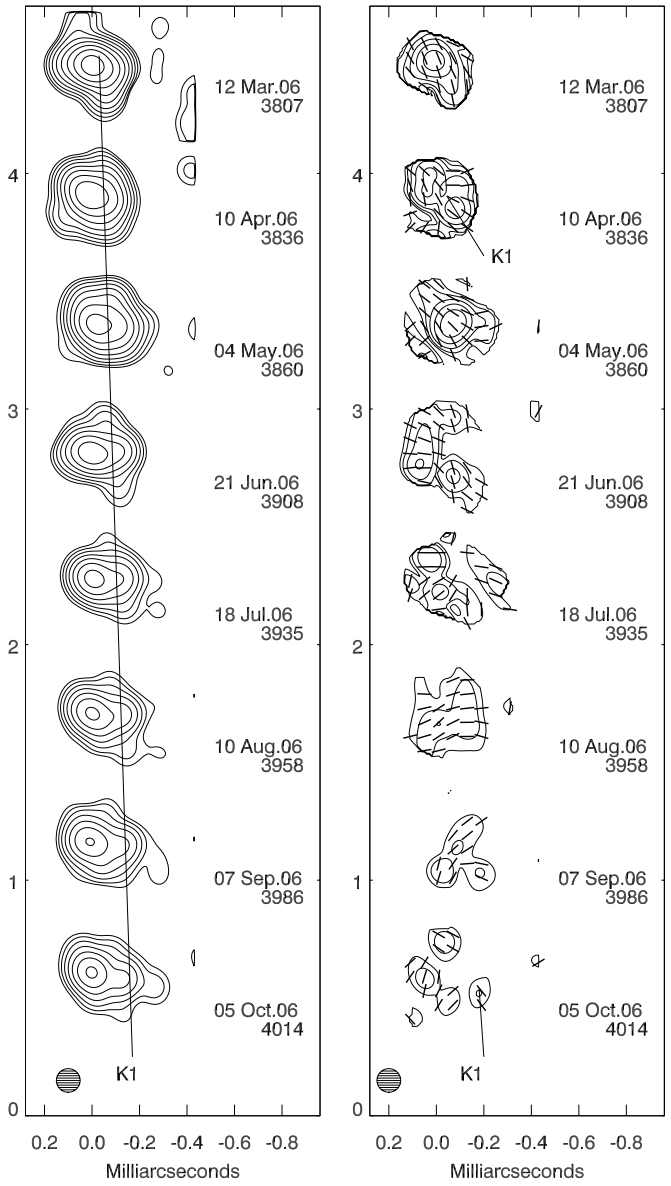

Figure 10. 43 GHz total (left) and polarized (right) intensity images of the quasar 3C 454.3 during period when $K1$ emerged from the core, $S_{\rm peak}$ = 8.25 Jy beam^{-1}, $S^{\rm p}_{\rm peak}$ = 0.241 Jy beam^{-1}, beam = 0.1 × 0.1 mas^2. Total intensity contours at 0.25%, 0.5%,... 64% of the peak and polarized intensity contours at 2%, 4%,... 64% of the peak. Sticks over the polarized intensity contours indicate the plane of polarization.

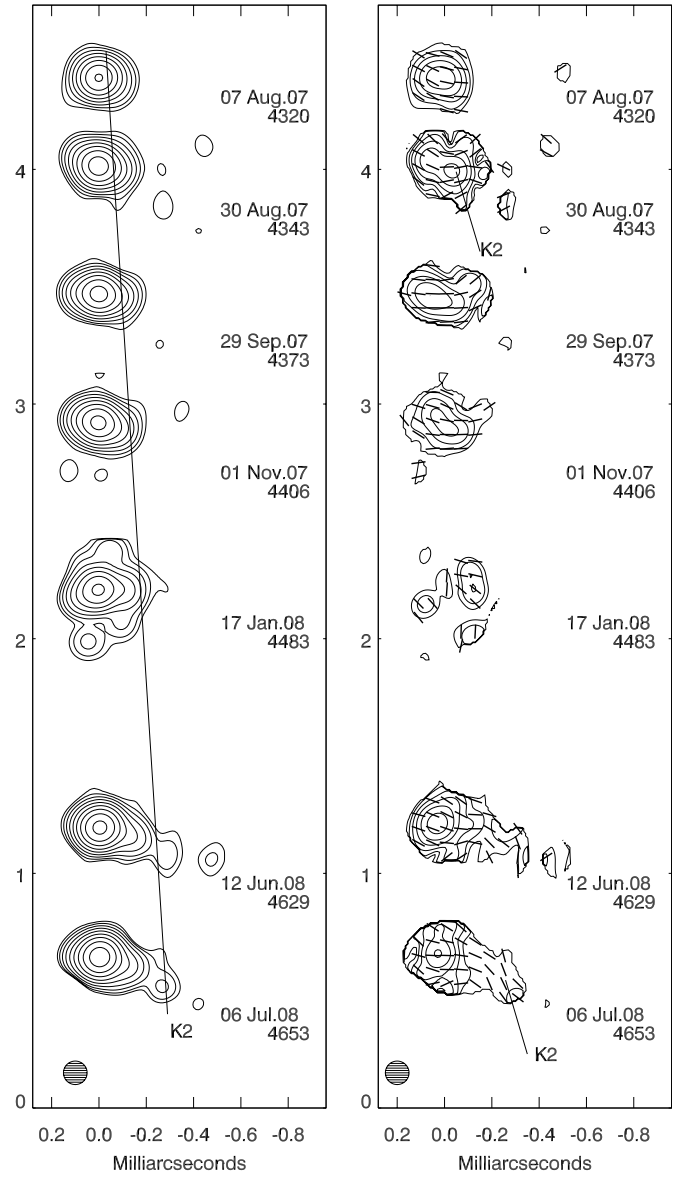

Figure 11. 43 GHz total (left) and polarized (right) intensity images of the quasar 3C 454.3 during period when $K2$ emerged from the core, $S_{\rm peak}$ = 15.69 Jy beam^{-1}, $S^{\rm p}_{\rm peak}$ = 0.268 Jy beam^{-1}. Total intensity contours at 0.25%, 0.5%,... 64% of the peak and polarized intensity contours at 2%, 4%,... 64% of the peak. Sticks over the polarized intensity contours indicate the plane of polarization.

et al. 2005). Table 1 lists for each knot the time of ejection, $T_\circ$, the highest flux density measured, $S^{\rm max}$, the epoch of $S^{\rm max}$, proper motion, μ, apparent speed, $\beta_{\rm app}$, Lorentz, Γ, and Doppler, δ, factors, and viewing angle, $\Theta_\circ$. There is a significant difference in the viewing angles of components $K2$ and $K3$, and the Lorentz and Doppler factors of $K3$ are twice those of $K1$ and $K2$, as well as twice those derived from the parameters of several components detected in 3C 454.3 between 1998 and 2001 (Jorstad et al. 2005). Figure 8 shows that the most dramatic change in the projected jet direction occurred after ejection of component $K3$. If we assume that the average jet parameters derived by Jorstad et al. (2005) give the most probable values of viewing and opening angles ($\Theta_\circ = 1.^\circ3$ and $\theta = 0.^\circ8$, respectively) then component $K3$ with $\Theta_\circ = 0.^\circ2$ should occupy the side of the jet closest to the line of sight, while component $K2$ with $\Theta_\circ = 2.^\circ5$ should move along the far side of the jet. Figure 8 supports such an interpretation, since, after the ejection of component $K2$, the projected jet direction swings to the north, while after the ejection of $K3$, $\Theta_{\rm jet}$ turns to the south. Component $K1$ appears to follow a path closer to the jet axis. In addition, Figure 8 shows a sharp swing of $\Theta_{\rm jet}$ near RJD ∼ 3750–3800, possibly indicating the emergence of a new knot from the core that we cannot distinguish from $K1$, which is bright and close to the core at this time (see Figure 7).

6. CORRELATION ANALYSIS BETWEEN HIGH-ENERGY VARIATIONS AND LIGHT CURVES AT OPTICAL AND MILLIMETER WAVELENGTHS

The X-ray observations were carried out less uniformly than observations at other wavelengths. There are three intervals when X-ray observations were obtained: I—RJD: 3502–3619, II—RJD: 4292–4450, and III—RJD: 4613–4858 (see Figure 2).

Table 1
Parameters of Moving Components

Knot	$T_\circ$ (yr)	$T_\circ$ RJD	$S_{\max}$ (Jy)	$T_{S_{\max}}$ RJD	μ (mas yr^{-1})	$\beta_{\rm app}$	Γ	δ	$\Theta_\circ$ (°)
(1)	(2)	(3)	(4)	(5)	(6)	(7)	(8)	(9)	(10)
$K1$	2005.50 ± 0.08	3553 ± 29	7.00 ± 0.34	3772	0.10 ± 0.02	4.9 ± 0.9	12.3	23.4	1.0
$K2$	2007.49 ± 0.07	4279 ± 25	3.81 ± 0.56	4343	0.18 ± 0.05	8.3 ± 2.3	10.7	17.6	2.5
$K3$	2007.93 ± 0.10	4439 ± 35	11.74 ± 0.52	4720	0.09 ± 0.03	4.1 ± 1.4	24.7	49.1	0.2

Notes. Columns: (1) name of component; (2) time of ejection from the core in years; (3) time of ejection from the core in RJD; (4) maximum flux of component; (5) epoch of the maximum flux of component; (6) proper motion; (7) apparent speed; (8) Lorentz factor; (9) Doppler factor; (10) viewing angle.

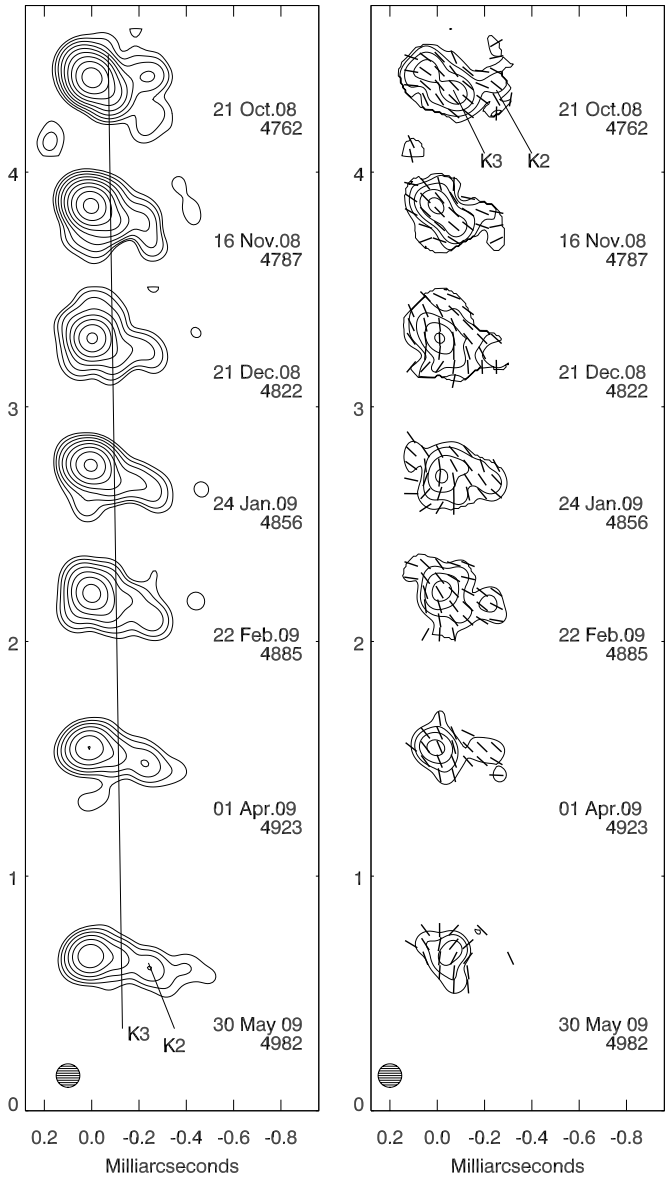

Figure 12. 43 GHz total (left) and polarized (right) intensity images of the quasar 3C 454.3 during period of $K3$ emerging from the core, $S_{\rm peak} = 14.28$ Jy beam^{-1}, $S^{\rm p}_{\rm peak} = 0.142$ Jy beam^{-1}, beam $= 0.1 \times 0.1$ mas^2. Total intensity contours at 0.25%, 0.5%,... 64% of the peak and polarized intensity contours at 2%, 4%,... 64% of the peak. Sticks over the polarized intensity contours indicate the plane of polarization.

We have performed correlation analysis between the X-ray, optical, and 230 GHz light curves separately for these intervals because (1) there are significant gaps in X-ray coverage between the intervals, (2) X-ray measurements at different intervals are obtained with different instruments, and (3) correlation between X-ray and longer-wavelength light curves can change with time (Chatterjee et al. 2008). For interval III, we include the *Fermi* γ-ray light curve in the correlation analysis. All light curves are grouped into one-day bins. We employ the code developed for correlation analysis (Chatterjee et al. 2008), which calculates the discrete cross-correlation function, CCF (Edelson & Krolik 1988), finds the peak of the CCF, $f_{\max}$, and determines the position of the centroid near the peak (White & Peterson 1994). This yields an estimate of the significance of the peak as well as the delay, τ, between variations at different wavelengths if the peak is significant at a confidence level 0.05.

Interval I has the best X-ray data sampling, provided by *RXTE* monitoring. We have correlated this X-ray light curve with the optical and 1 mm light curves over exactly the same period, while performing the correlation between the *R* band and 230 GHz light curves over a longer period, RJD: 3499–3750, which has similar sampling at the two wavelengths. Figure 13 (left panel) gives the results of the CCF analysis, revealing very strong correlation between variations at X-ray and longer wavelengths. During interval II, there are only 21 measurements obtained with *Swift*, insufficient for correlation analysis. We compute the CCF only between the optical and 230 GHz light curves for the period RJD: 4200–4505. Figure 13 (right panel) shows a moderate correlation between variations at the two wavelengths. During interval III, the X-ray (*Swift*), optical, and 230 GHz light curves have good coverage, with 72, 137, and 115 points, respectively; daily γ-ray fluxes became available starting at RJD: 4684. We have added γ-ray measurements from RJD: 4649–4675 presented in Figure 1 of Abdo et al. (2009b) to the γ-ray light curve for correlation analysis between γ-ray and optical variations. In the case of the X/γ-ray correlation, the γ-ray data during RJD: 4649–4675 are not used due to the absence of X-ray measurements during this period (see Figure 2). Figure 14 (left panel) presents the CCFs between X-ray, optical, and 230 GHz light curves, while the right panel shows the CCF between the γ-rays and lower frequencies. Table 2 summarizes the results of the correlation analysis for all intervals and wavelengths.

Table 2 shows a strong correlation between optical and 230 GHz variations with a delay of millimeter-wave emission with respect to the optical variations. Time lags between the optical and 1 mm light curves decrease significantly, from ~50 days to ~10 days, from interval I to III, respectively. Raiteri et al. (2008b) have reported a change in delay between the optical and 230 GHz light curves of the quasar during 2007–2008 relative to 2005–2007, consistent with the difference in $\tau_{\rm opt/230}$ that we find between intervals I and II. During interval III, the delay became even shorter. Analysis of the X-ray/optical correlation suggests that variations at the two wavelengths are simultaneous within

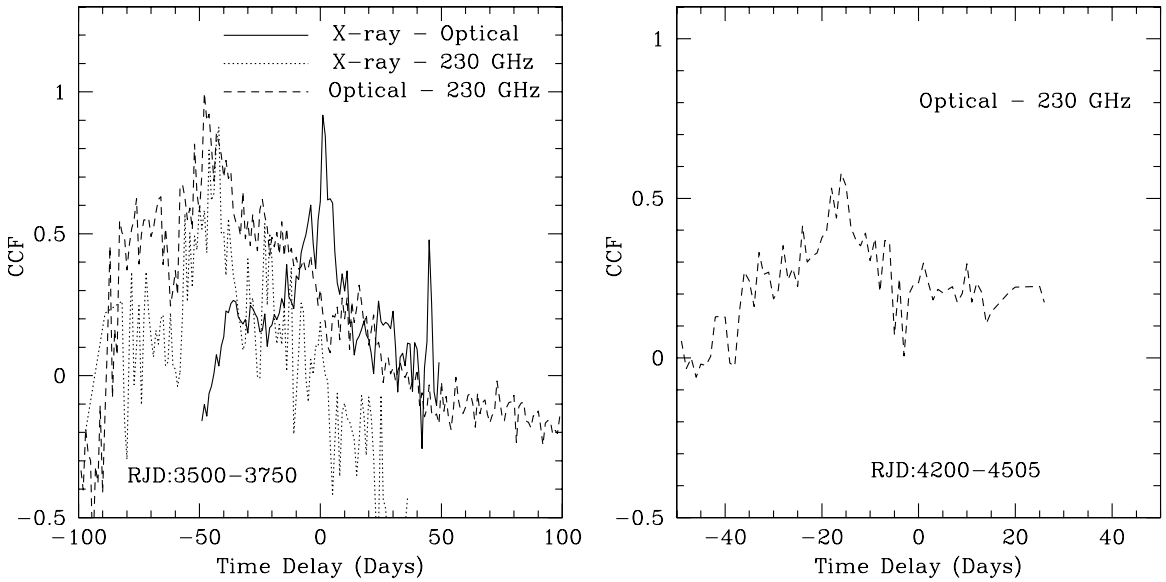

Figure 13. Cross-correlation function between X-ray, optical, and 230 GHz light curves for the indicated time intervals. A negative delay corresponds to higher frequency variations leading.

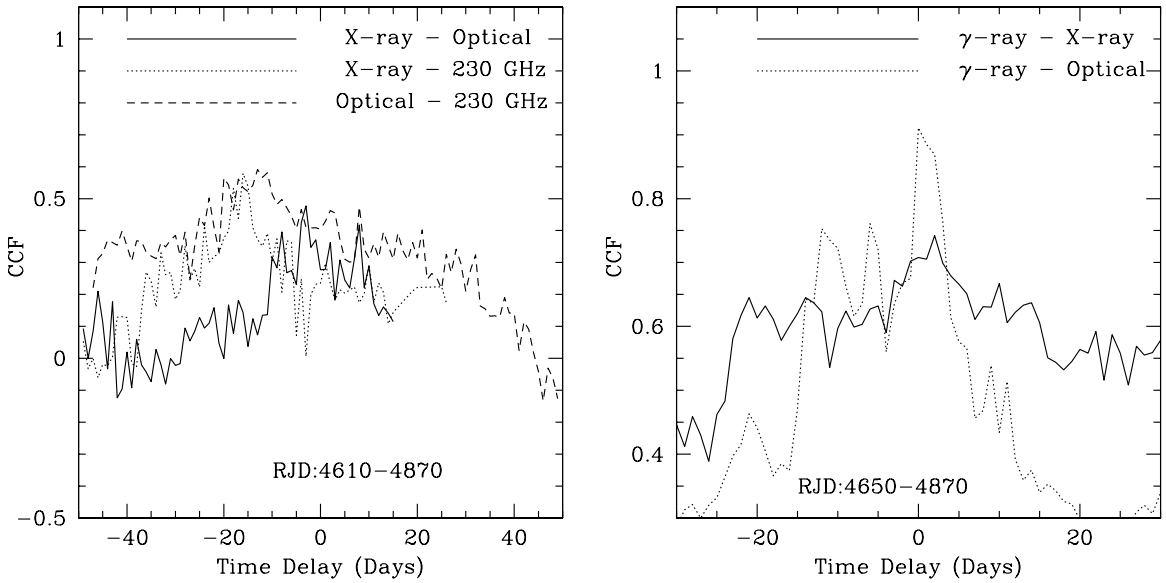

Figure 14. Left: cross-correlation function (CCF) between X-ray, optical, and 230 GHz light curves for the time interval RJD: 4610–4860. Right: CCF between γ/X-ray variations for the time interval RJD: 4689–4870, and between γ-ray and optical light curves for the time interval RJD: 4650–4870. A negative delay corresponds to higher frequency variations leading.

Table 2
Results of Correlation Analysis

Waves	RJD: 3502–3619		RJD: 4292–4450		RJD: 4613–4858	
	f_{max}	τ (days)	f_{max}	τ (days)	f_{max}	τ (days)
(1)	(2)	(3)	(4)	(5)	(6)	(7)
γ-ray/X-ray	...	...	...	...	+0.75	$+2 \pm 3$
γ-ray/opt	...	...	...	...	+0.91	$+0 \pm 1$
X-ray/opt	+0.92	$+1 \pm 1$	...	...	+0.48	-3 ± 2
X-ray/230	+0.88	-42 ± 3	...	...	+0.58	-16 ± 3
Opt/230	+0.98	-48 ± 5	+0.46	-21 ± 2	+0.59	-13 ± 4

Notes. Columns: (1) two bands used for correlation analysis; (2, 4, 6) f_{max}—maximum coefficient of linear correlation; (3, 5, 7) τ—time delay between the two bands at the maximum coefficient, negative delay corresponds to higher frequency variations leading.

1 day. However, a change from positive (optical variations lead) to negative (X-rays lead) delay might have taken place from interval I to interval III, although we judge this to be of low significance given the uncertainties of the delays. Nevertheless, such a possibility is supported by the X-ray/230 GHz delays as well: during interval I, the X-ray/230 GHz delay is shorter than the delay between the optical and 230 GHz light curves; the opposite situation ($|\tau_{opt/230}| > |\tau_{x/230}|$) is observed for interval III, but again the differences are within the uncertainties of τ.

Interval III is especially interesting, since it contains the *Fermi* γ-ray light curve. The γ-ray variations show the best correlation with the optical light curve, with no delay exceeding 1 day (Figure 14, right panel), in agreement with the findings of Bonning et al. (2009). However, these authors reported the absence of a correlation between γ- and X-rays, while our analysis indicates the presence of such a correlation, although the peak of the CCF is less prominent than that between the

Table 3
Parameters of Total Flux Outbursts

Name	Optical			230 GHz			37 GHz		
	T_{opt} RJD	E_{opt} (mJy day)	w_{opt} (days)	T_{230} RJD	E_{230} (Jy day)	w_{230} (days)	T_{37} RJD	E_{37} (Jy day)	w_{37} (days)
(1)	(2)	(3)	(4)	(5)	(6)	(7)	(8)	(9)	(10)
O_{K1}/M_{K1}	3501 ± 1	2194	47	3534 ± 5	9343	104	3700 ± 5	6200	180
	3537 ± 1	166	15	...	...	...	...	...	...
	3561 ± 1	115	18	...	...	...	...	...	...
	3673 ± 1	96	19	...	...	...	...	...	...
$M1$	...	...	...	3781 ± 5	1140	38	3788 ± 5	528	24
O_{K2}/M_{K2}	4301 ± 1	373	19	4330 ± 5	1985	50	4331 ± 5	1871	104
	4334 ± 1	170	12	...	...	...	...	...	...
	4382 ± 1	113	16	...	...	...	...	...	...
O_{K3}/M_{K3}	4437 ± 1	410	16	4454 ± 5	1020	51	4450 ± 5	2090	64
	4491 ± 1	253	27	...	...	...	...	...	...
	4661 ± 1	164	16	...	...	...	...	...	...
$M2$	...	...	...	4705 ± 5	6810	134	4707 ± 5	6663	155

Notes. Columns: (1) designation of outburst; (2–4) epoch of the peak, power, and timescale of optical outburst, respectively; (5–7) epoch of the peak, power, and timescale of outburst at 230 GHz, respectively; (8–10) epoch of the peak, power, and timescale of outburst at 37 GHz, respectively; uncertainties of the epochs of peaks correspond to the smoothing time of light curves.

γ-ray and optical light curves. From this analysis, we conclude that the γ/X-ray variations are simultaneous within 2 days. Our X- and γ-ray light curves include additional data after RJD: 4750, which probably explains the discrepancy between our correlation result and that obtained by Bonning et al. (2009).

We have performed correlation analysis between the 230 GHz and 37 GHz light curves using all data from RJD: 3000 to RJD: 4850 (see Figure 1). The CCF between the two wavelengths presented in Figure 15 shows a global maximum with a delay $\tau_{230/37} = -215 \pm 30$ days and two local maxima at $\tau_{230/37} = -73 \pm 30$ days and $\tau_{230/37} = 0 \pm 10$ days. This is connected with a change of the delay between the variations at the two wavelengths with time. Indeed, the CCF for the period from RJD: 4000 to RJD: 4850, which excludes the largest millimeter-wave outburst, gives a well defined peak at $\tau_{230/37} = 0 \pm 7$ days (Figure 15, dotted line). The change of the delay between the 230 GHz and 37 GHz light curves from ~200 days to 0 days reflects the transition of millimeter-wave emission of the source from optically thick to optically thin (see Section 8), which also leads to a decrease of the delay between optical and millimeter-wave variations.

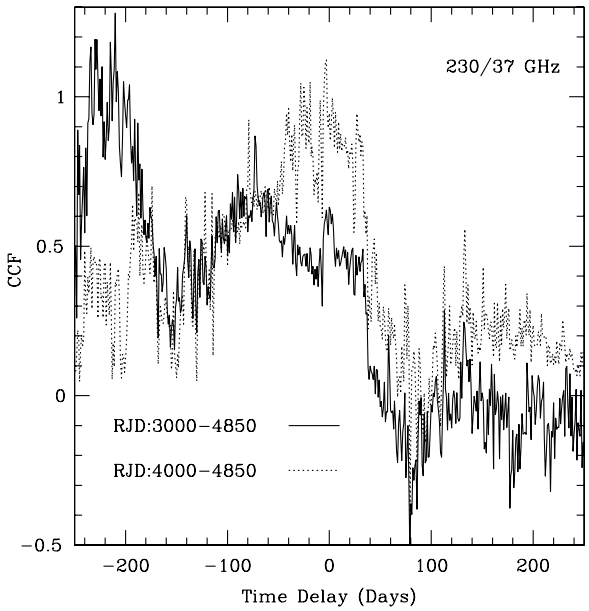

Figure 15. Cross-correlation function between the 230 GHz and 37 GHz light curves for periods RJD: 3000–4850 (solid line) and RJD: 4000–4850 (dotted line).

7. COMPARISON OF TIMING OF FLUX VARIABILITY AND EJECTION OF SUPERLUMINAL COMPONENTS

We decompose the light curves at optical and radio wavelengths into individual flares with exponential rise and decay by applying the method of Valtaoja et al. (1999; see also Chatterjee et al. 2008). The R-band light curve is smoothed with 1-day binning, while the millimeter-wave curves are smoothed with 5-day binning. The method gives the epoch of peak flux, T_ν, output power, E_ν (area under the curve fitting a flare), and width, w_ν (average of the rise and decay times). The decomposition yields 10 outbursts in the R-band light curve and five outbursts in the millimeter-wave curves, each with $w_\nu > 10$ days (Table 3). We consider these to be the most reliable flares, based on the sampling of the data. We have cross-identified outbursts at different wavebands by assuming that events associated with each other should have a difference in times of the peaks corresponding to the delay found from the correlation analysis of light curves at the two wavelengths, i.e., $T_{\nu_1} - T_{\nu_2} \approx \tau_{\nu_1,\nu_2}$ (see Section 6).

We also analyzed relative values of the parameters E_ν and w_ν to find additional support for the cross-identification. This implies, for example, comparison of E_{opt}/E_{opt}^{max} with E_{230}/E_{230}^{max}, where E_{opt}^{max} and E_{230}^{max} are the maximum output powers derived among optical and millimeter-wave outbursts, respectively. The results of cross-identification are shown in Table 3. We have associated the optical outbursts peaked at RJD: 3501, RJD: 4301, and RJD: 4437 with the 230 GHz outbursts with maxima at RJD: 3534, RJD: 4330, and RJD: 4454, respectively, because differences in the peaks (−33, −29, and −17 days) agree very well with the delays found between the two wavelengths (Table 2). The rest of the optical flares do not have counterparts at mm wavelengths. All 230 GHz outbursts have corresponding 37 GHz outbursts, based on the results of the correlation analysis.

Table 4
Connection between Ejection and Peak of Outbursts

Knot	$\Delta T_{\rm opt}$ (days)	ΔT_{230} (days)	ΔT_{37} (days)
(1)	(2)	(3)	(4)
K1	-52 ± 30	-19 ± 34	147 ± 34
K2	22 ± 26	51 ± 30	52 ± 30
K3	-2 ± 36	15 ± 40	11 ± 40

Notes. Columns: (1) name of component; (2–4) delay of the peak of optical, 230 GHz, and 37 GHz outburst, respectively, with respect to the ejection time of component, $\Delta T_\nu = T_\nu - T_\circ$.

We have also related the millimeter-wave outbursts to the ejection of superluminal knots, based on the assumption that an outburst and an ejection are connected if the latter occurs within the width of the outburst. Table 4 gives the delays between the time of the ejection and the peak of the corresponding outburst at different wavelengths, $\Delta T_\nu = T_\nu - T_\circ$. It shows that each ejection occurred within 20–30 days of the peak of a 230 GHz outburst. We denote the 230 GHz outbursts as M_{K1}, M_{K2}, and M_{K3} in accordance with the designation of related superluminal component (Figure 1). We then associate a newly appearing superluminal knot with an optical outburst if the latter is related to a millimeter-wave outburst. As a result, the three major optical outbursts with the highest power are associated with newly emerging superluminal components. We denote these optical outbursts as O_{K1}, O_{K2}, and O_{K3} in a similar manner as the millimeter-wave outbursts connected with the ejections (see Figure 1 and Table 3).

Analysis of Tables 3 and 4 reveals that (1) all ejections trigger an increase in optical and millimeter-wave activity, (2) the connection between optical outbursts and ejections of superluminal components is not one to one, since either one ejection can trigger multiple optical outbursts or there are optical outbursts that are not connected with a new knot, and (3) all ejections occur during the rising branch of a 37 GHz outburst, as previously reported by Savolainen et al. (2002). In the case of the $K1$ event, there is a pattern that the strongest optical outburst is followed by the 230 GHz outburst and by the ejection of a superluminal knot from the 43 GHz core. The delays between the peaks of the outbursts and time of ejection of the knot can be interpreted in terms of spatial separation of sites of the outbursts with respect to the core. In the case of events $K2$ and $K3$, such an interpretation is possible as well, taking into consideration uncertainties in ΔT_ν. However, another interpretation, which better corresponds to the derived delays and reflects the differences in properties of O_{K2} and O_{K3} with respect to O_{K1}, suggests that the sites of both the optical and 230 GHz outbursts are located in the millimeter-wave core and that the outbursts occurred during the ejection of a superluminal knot. A delay between the peaks of associated optical and 230 GHz outbursts can be caused by the difference in time when the maximum number of relativistic electrons radiating at optical and millimeter waves was achieved: the time of the maximum number of relativistic electrons accelerated to optical-emitting energies coincides with the ejection time, while acceleration of electrons to millimeter-wave-emitting energies continues for 20–30 days longer.

The extensive optical data collected by the WEBT collaboration (Raiteri et al. 2008b) contain a number of epochs with several measurements during a single date. These authors have noted strong intraday variability in 3C 454.3 in the optical

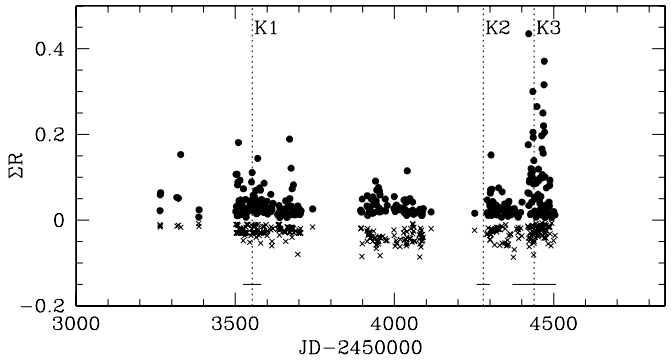

Figure 16. Values of standard deviation of R-band magnitudes averaged within a day (filled circles). The average uncertainties of individual measurements within a day are shown by crosses and are given negative values to distinguish them from the standard deviations. Dotted lines show times of ejections of superluminal components.

R band on a timescale of $t_{\rm var} \sim 1.5$ hr in 2007 December. We have calculated the means and standard deviations for R magnitudes for each Julian date with seven or more measurements. Figure 16 presents the standard deviations, ΣR, versus epoch, along with the average uncertainty for individual measurements on a given date, σR. There is possible intraday variability during the ejection of component $K1$, and pronounced intraday variability during the emergence of knot $K3$. According to our estimations, component $K3$ has the highest Doppler factor that we observed in the jet of 3C 454.3 from 2005 to 2009. This supports the idea that the knot is responsible for the short timescale of the variability seen at optical wavelengths. The angular size of the region that can produce such a variability is $a_{\rm var} \lesssim c\Delta t_{\rm var}(1+z)/(\delta D_{\rm A}) \approx 10^{-9}$ arcsec, where $D_{\rm A}$ is the angular distance to 3C 454.3. The size of $K3$ that we adopt from the VLBA imaging is $\sim 10^4$ larger than $a_{\rm var}$. However, analysis of polarization properties in quasars (Jorstad et al. 2007; D'Arcangelo et al. 2007) shows that the polarized optical emission, although partially co-spatial with the millimeter-wave core, occupies a volume that is thousands of times less than does the polarized emission at 43 GHz. Therefore, it is possible that the site of an optical flare lies within a superluminal knot passing through the core, and is confined to such a small region in the knot that it can vary on extremely short timescales.

8. SPECTRAL BEHAVIOR

We use 340 GHz, 230 GHz, 86 GHz, and 37 GHz data to calculate millimeter-wave spectral indices, $\alpha_{\rm mm}$ ($S_\nu \propto \nu^{-\alpha}$). The spectral index for a given Julian date was calculated if there were measurements at a minimum of three wavelengths within 2 days of the date. When there were several measurements over a short time period, the observations nearest to each other were used. Figure 17 reveals that the millimeter-wave spectral index exhibited significant variability. The uncertainty in $\alpha_{\rm mm}$ reflects the scatter about the best-fit power law. During a quiescent state $\alpha_{\rm mm}$ is typical of a compact, flat-spectrum radio source, $\alpha^q_{\rm mm} = 0.18 \pm 0.04$, where $\alpha^q_{\rm mm}$ denotes a quiescent state chosen during the period RJD: 3900–4200 (Figure 1) and denoted by QS. The spectrum became strongly inverted during outburst O_{K1} and slightly inverted during outburst O_{K2}. The spectral index reaches a local minimum at epochs of superluminal ejections. After an ejection, $\alpha_{\rm mm}$ changes sharply, rising to the value of $\alpha^{\rm q}_{\rm mm}$, and then continuing to increase up to a value $\alpha_{\rm mm} = 0.5$–0.6, signifying that the emission is close to being optically thin. The epochs of the two global maxima of $\alpha_{\rm mm}$

Table 5
Optical, Near-IR, UV, and X-ray Spectral Indices[a] of the Synchrotron Emission Components

State	α_{IR}^{syn}	α_{opt}^{syn}	α_{UV1}^{syn}	α_{UV2}^{syn}	α_x	$Epoch_x$ (RJD)
(1)	(2)	(3)	(4)	(5)	(6)	(7)
O_{K1}^{b}	1.88 ± 0.03	1.67 ± 0.11	...	...	0.72 ± 0.04	3505.5814
O_{K2}+O_{K3}	1.31 ± 0.02	1.68 ± 0.01	2.31 ± 0.14	0.81 ± 0.17	...	...
O_{K2}	...	...	...	...	0.41 ± 0.13	4299.1418
O_{K3}	...	...	...	...	0.56 ± 0.12	4426.7780
$M2$	1.65 ± 0.02	1.64 ± 0.01	2.33 ± 0.22	1.16 ± 0.15	0.66 ± 0.18	4706.2752
QS[c]	1.42 ± 0.01	1.97 ± 0.03	...	...	0.57 ± 0.01	4087.5

Notes. Columns: (1) state of activity; (2) IR spectral index of a synchrotron component; (3) optical spectral index of a synchrotron component; (4) UV (2500–3500 Á) spectral index of a synchrotron component; (5) UV (2000–2500 Á) spectral index of a synchrotron component; (6) X-ray (2.4–10 keV) spectral index; (7) epoch of α_x measurement.
[a] All spectral indices are defined as $S_\nu \propto \nu^{-\alpha}$.
[b] The values of α_{opt} and α_{ir} are from Hagen-Thorn et al. (2009).
[c] The values of α_x are from Raiteri et al. (2007).

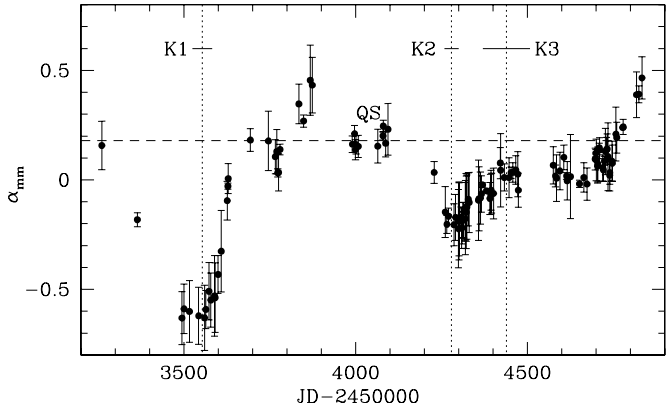

Figure 17. Spectral index at 230–37 GHz (1–8 mm). Dashed line shows α_{mm} during a quiescent state, QS. Dotted lines show times of ejections of superluminal components and solid line segments show uncertainties in the ejection times.

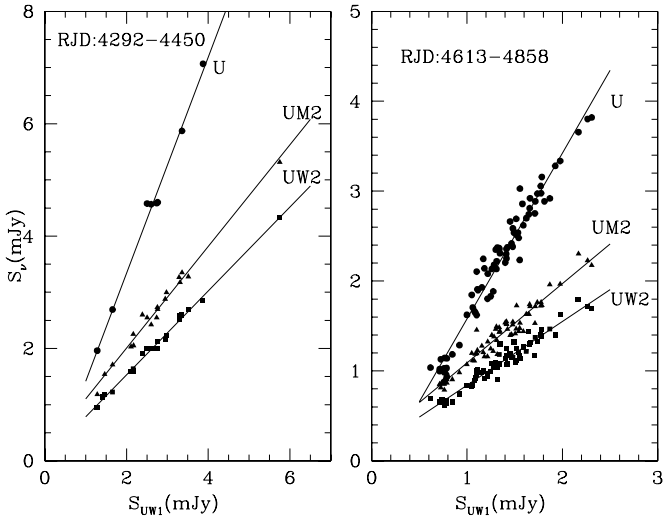

Figure 18. Flux–Flux dependences for UVOT bands for periods RJD: 4292–4450 (left) and JD: 4613–4858 (right).

coincide with the peaks of the sharp millimeter-wave outbursts at RJD: 3781 ($M1$) and RJD: 4705 ($M2$), which are identified neither with optical outbursts nor with ejections of superluminal components (Table 3, Figure 1). The peaks of $M1$ and $M2$ do, however, coincide with the epochs of maximum 43 GHz flux of knots $K1$ and $K3$, respectively (Table 1).

Raiteri et al. (2007, 2008a, 2008b) plot the SEDs of the quasar at different brightness levels. These authors interpret the behavior of the optical–UV part of the spectrum as a result of superposition of beamed jet emission, blended line emission from the broad-line region (little blue bump), and emission from the accretion disk (big blue bump), which agrees with previous findings by Smith et al. (1988). The compound SED explains the flattening of the spectrum with a decrease in brightness, since at a low emission state the contribution of the blue bumps becomes more pronounced. We use the method suggested by Hagen-Thorn (1997) to determine the spectral characteristics of a component of the source responsible for flux variability observed on timescales of days and weeks. Such a component most likely originates via the synchrotron mechanism and has a power-law SED from IR to UV wavelengths. The method allows one to determine spectral indices of the synchrotron emission separately from the thermal emission, which varies on much longer timescales. The detailed description of the method and its application to multifrequency optical and near-IR data for the event O_{K1} are given in Hagen-Thorn et al. (2009). We have performed a similar analysis for other events. Table 5 gives the near-IR and optical spectral indices of synchrotron components during outbursts O_{K1}, O_{K2} + O_{K3}, and $M2$, as well as the quiescent period QS. Outbursts O_{K2} and O_{K3} are combined owing to the small number of multifrequency optical and IR observations obtained separately for each outburst.

We have derived spectral indices of synchrotron components in the UV region, applying the same method to multifrequency *Swift* UVOT measurements. We have constructed relations between fluxes in U, $UM2$, and $UW2$ bands relative to fluxes in $UW1$ band, with the largest number of measurements, during two periods RJD: 4292–4450 (O_{K2} + O_{K3}) and RJD: 4613–4858 ($M2$), when multifrequency UV data were available (see Figure 1). Figure 18 shows the flux–flux dependences, which can be fit by straight lines, $S_i = A_i + B_i S_{UW1}$. The slopes of the regressions, B_i, are used to construct the relative SED of the synchrotron component responsible for the variability. Figure 19 shows the relative SEDs of synchrotron components at the UV bands along with the those obtained for IR and optical parts of the electromagnetic spectrum (Table 5). The relative UV SEDs are very similar during both events. However, they cannot be represented by a single power law owing to significant flattening of the spectrum at wavelengths below 2630 Å. We have determined the spectral indices for the soft UV (2634–3500 Å), α_{UV1}^{syn}, and for the hard UV (2030–2634 Å), α_{UV2}^{syn}, emission separately

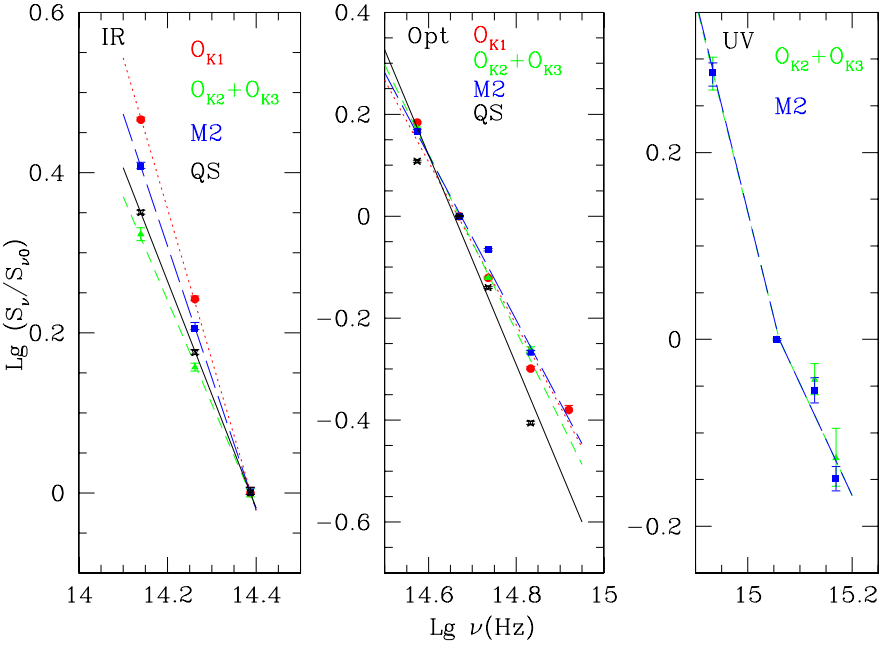

Figure 19. Near-IR (left), optical (middle), and UV (right) relative spectral energy distributions of synchrotron emission from 3C 454.3, normalized to *J* band (Lg($\nu_\circ$) = 14.387), *R* band (Lg($\nu_\circ$) = 14.670), and *UW1* band (Lg($\nu_\circ$) = 15.056), respectively, during different events.

(Table 5). We stress that this hardening of the UV spectrum cannot be connected to the contribution of the blue bumps to the SED owing the short timescale of variability of the emission.

Figure 19 and Table 5 show that the optical spectra of the variable components are similar at the flaring states and flatter than $\alpha^{\rm q}_{\rm opt}$. This is a characteristic of optical variability often observed in blazars (e.g., Larionov et al. 2008): variable sources are bluer at brighter flux levels. In the quiescent state, $\alpha^{\rm q}_{\rm IR}$ is flatter than $\alpha^{\rm q}_{\rm opt}$ by ∼0.5, as expected for a synchrotron source with relativistic electron energy distribution $N(E) = N_\circ E^{-3.8}$ when optically emitting electrons suffer strong radiative losses. The significantly steeper $\alpha^{\rm syn}_{\rm IR}$ with respect to $\alpha^{\rm syn}_{\rm opt}$ during event O_{K1} is unusual. This effect can be caused by undersampling the IR data during the brightest stage of optical emission (see Figure 1). However, if it is real, a hardening of the synchrotron spectrum can occur at electron energies where Klein–Nishina (KN) effects become important (Dermer & Atoyan 2002; Moderski al. 2005), if inverse Compton losses dominate over synchrotron losses, i.e., $u_{\rm phot} \gg B^2/(8\pi)$, where $u_{\rm phot}$ is energy density of the photon field and B is strength of the magnetic field. Such a condition might occur during the dramatic outburst O_{K1} that yields diminishing inverse Compton losses at frequencies $\nu \geqslant 2.6\times10^{15}\delta B/(1+z)(\nu'/10^{15})^{-2}$ Hz, where $\nu' \approx \Gamma\nu_{\rm seed}$ and $\nu_{\rm seed}$ is the frequency of the external photon field. If we assume that δ and Γ correspond to knot $K1$ and $\nu_{\rm seed} \approx 5\times10^{13}$ Hz, a hardening of the synchrotron spectrum at optical wavelengths, $\nu \geqslant 4\times10^{14}$ Hz, requires the magnetic field $B \approx 4.5$ mG, while for $B \approx 1$ G the external photon field should peak in U band, $\nu_{\rm seed} \approx 7.5\times10^{14}$ Hz.

The soft UV spectrum is steep, with $\alpha^{\rm syn}_{\rm UV} \approx 2.3$, an even steeper synchrotron spectral index at 2500 Å, ∼2.7, was derived by Smith et al. (1988) from multifrequency polarization data of 3C 454.3. The hardening of the synchrotron UV spectrum beyond 2500 Å that we observe during events O_{K2}+O_{K3} and $M2$ can be caused by inverse Compton losses in the KN regime, as described above. According to the SED presented by Abdo et al. (2009b), the inverse Compton peak exceeds the synchrotron peak during $M2$ event by at least a factor of ∼5,

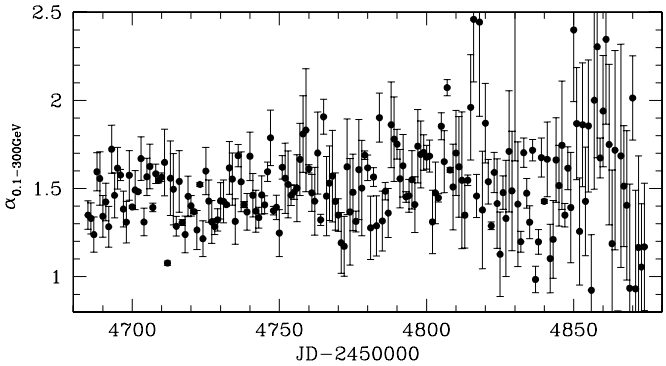

Figure 20. Spectral index at 0.1–300 GeV.

which implies that the conditions for inverse Compton losses should be achieved (Moderski al. 2005). For events O_{K2}+O_{K3} and $M2$, the jet parameters are uncertain. We adopt the average jet parameters $\Gamma = 16$ and $\delta = 25$ (Jorstad et al. 2005) that result in a hardening of the synchrotron spectrum at $\nu \geqslant 2\times10^{15}$ if $\nu_{\rm seed} \approx 3\times10^{15}$ Hz and $B \approx 50$ mG or if $B \approx 1$ G and $\nu_{\rm seed} \approx 2\times10^{14}$ Hz.

X-ray spectral indices at 2.4–10 keV were calculated in the process of the *RXTE* data reduction. We use the X-ray spectral index from the epoch closest to the time of the peak of O_{K1} to characterize the outburst. For outbursts O_{K2}, O_{K3}, and $M2$, we have derived $\alpha_{\rm x}$ at 2.4–10 keV from *Swift* data obtained at epochs closest to the dates of the peaks of the outbursts using the same spectral model as for the *RXTE* data. The X-ray spectral index for the quiescent state is from Raiteri et al. (2007), derived from *XMM-Newton* measurements on 2006 December 18/19. Table 5 summarizes the X-ray spectral indices and shows that during outbursts O_{K2} and O_{K3} $\alpha_{\rm x}$ is similar to that in the quiescent state, while during the most powerful optical outburst, O_{K1}, $\alpha_{\rm x}$ became steeper than $\alpha^{\rm q}_{\rm x}$.

We have determined γ-ray spectral indices, $\alpha_{0.1-300\,\rm Gev}$, using a single power-law model. Figure 20 shows variations of the γ-ray spectral index during RJD: 4684–4873. The average value

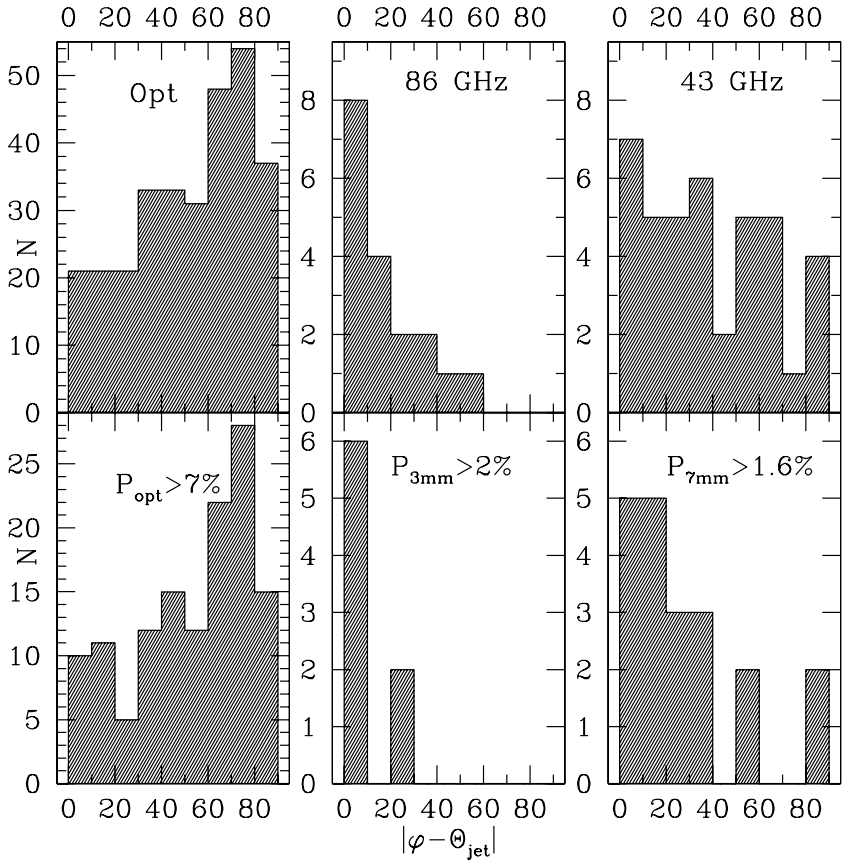

Figure 21. Distributions of position angle of polarization with respect to the jet direction at different wavelengths for all (top panels) and high polarization (bottom panels) measurements; values of $\varphi_{7\,\mathrm{mm}}$ are corrected for RM according to Jorstad et al. (2007).

$\langle\alpha_{0.1-300\,\mathrm{Gev}}\rangle = 1.46 \pm 0.29$ corresponds to the optical and near-IR spectral indices of the synchrotron component during outburst $M2$. Abdo et al. (2009b) have found that the γ-ray spectrum of 3C 454.3 during $M2$ event is described by a broken power-law model with $\alpha_\gamma^{\mathrm{low}} = 1.27 \pm 0.12$ and $\alpha_\gamma^{\mathrm{high}} = 2.50 \pm 0.35$ and a break at 2.4 ± 0.6 GeV. This implies a close correspondence between $\alpha_\gamma^{\mathrm{low}}$ and the average of α_{mm} and $\alpha_{\mathrm{opt}}^{\mathrm{syn}}$ and between $\alpha_\gamma^{\mathrm{high}}$ and the spectral index of soft synchrotron UV emission, $\alpha_{\mathrm{UV1}}^{\mathrm{syn}}$ (see Table 5).

9. POLARIZATION BEHAVIOR

Figure 3 shows the parameters of the polarization from the whole source at both optical wavelengths and 86 GHz, and at 43 GHz in the VLBI core region. The data reveal a very wide range of variability of the degree of optical polarization, from ∼0% to 30%. The range and timescale of the variability decrease with wavelength, in agreement with the findings of Jorstad et al. (2007). The average values of the degree of polarization are $\langle p_{\mathrm{opt}}\rangle = 7.4\% \pm 5.3\%$, $\langle p_{86}\rangle = 2.3\% \pm 1.4\%$, and $\langle p_{43}\rangle = 1.6\% \pm 0.8\%$. At all three wavelengths, the P.A. of polarization covers the entire range from -180° to 0°, although φ_{opt} varies more rapidly than that of the millimeter emission. We have collected 253 simultaneous measurements of the optical flux and degree of polarization, which produce a statistically significant correlation between these parameters (linear coefficient of correlation, $\rho = 0.32$). The connection between the flux and degree of polarization is weaker in the 43 GHz core ($\rho = 0.21$) and absent at 86 GHz ($\rho = 0.05$).

We have constructed distributions of alignment of EVPAs at optical and 86 GHz wavelengths from the whole source, and at 43 GHz from the VLBI core region with respect to the jet direction. The distributions are presented in Figure 21 for the all measurements at each frequency, as well as for cases when the degree of polarization is higher than the average at a given frequency. The optical and 43 GHz core EVPAs extend across all possible directions with respect to the jet axis, although φ_{opt} tends to be perpendicular to the jet, while φ_{43} aligns more often with the jet direction. These tendencies are more prominent when the degree of polarization is high. This might be partially caused by the larger uncertainties in EVPA when p is low. The EVPA at 86 GHz maintains good alignment with the jet direction independent of degree of polarization. However, this evidence of better alignment may be biased by the poorer time coverage at 86 GHz since, in general, Figure 3 shows good agreement between the EVPA measurements at 86 and 43 GHz.

Table 6 presents the optical polarization P.A. and EVPA in the 43 GHz core for essentially simultaneous observations (within a week, less than the timescale of significant variability at 43 GHz). The optical and 86 GHz polarization P.A.s measured within 2 days of each other are listed in Table 7. There are 19 simultaneous pairs of optical and 43 GHz measurements, with 8 pairs (42%) showing alignment between φ_{opt} and φ_{43} within the 1σ uncertainty of the measurements. The optical and 86 GHz EVPAs agree in only 2 out of 12 pairs (17%). Alignment between φ_{opt} and φ_{43} is observed independently of direction of polarization with respect to the jet axis, while two cases of agreement between φ_{opt} and φ_{86} occur when the EVPAs are close to the jet direction. If optical and 43 GHz EVPAs are

Table 6
Quasi-simultaneous Optical and 43 GHz Polarization Measurements

Epoch^{a}_{opt} (RJD) (1)	p_{opt} (%) (2)	φ_{opt} (deg) (3)	Epoch_{43} (RJD) (4)	p_{43} (%) (5)	φ^{b}_{43} (deg) (6)	Θ_{jet} (deg) (7)
*3563.4871	4.90 ± 0.20	−134.4 ± 1.1	3568	1.0 ± 0.2	−127.0 ± 4.4	−94.8 ± 3.4
3656.3266	10.72 ± 1.45	−145.9 ± 3.9	3650	1.7 ± 0.3	−95 ± 4.9	−98.4 ± 4.4
3684.2745	8.09 ± 2.06	−21.3 ± 7.3	3689	0.8 ± 0.2	7.1 ± 4.6	−89.0 ± 5.3
3697.3281	9.89 ± 1.99	−26.1 ± 5.8	3695	2.1 ± 0.4	9.5 ± 2.9	−101.2 ± 7.5
3729.2215	8.93 ± 0.58	17.1 ± 1.9	3726	2.2 ± 0.2	−0.5 ± 2.4	−86.6 ± 3.3
*3906.4829	6.46 ± 3.50	−114.6 ± 15.6	3908	1.8 ± 0.3	−136.7 ± 5.5	−90.9 ± 2.9
3932.5166	12.10 ± 6.53	−59.3 ± 15.5	3935	1.6 ± 0.5	−92.3 ± 8.4	−90.6 ± 2.0
*4014.3535	15.83 ± 6.40	−30.5 ± 11.6	4014	1.1 ± 0.5	−22.5 ± 14.4	−101.0 ± 4.6
*4050.7222	2.00 ± 0.70	−53.3 ± 10.0	4057	1.4 ± 0.5	−49.0 ± 10.7	−100.4 ± 5.3
4086.1988	9.31 ± 0.82	−161.9 ± 2.5	4087	0.6 ± 0.5	−67.9 ± 22.8	−94.7 ± 2.1
*4269.4898	2.66 ± 1.09	−124.1 ± 11.8	4266	0.7 ± 0.2	−126.0 ± 5.9	−86.7 ± 6.5
*4300.4824	21.44 ± 0.24	−100.8 ± 0.6	4294	2.6 ± 0.3	−97.0 ± 3.4	−86.9 ± 4.7
4319.4380	5.76 ± 0.61	−58.2 ± 3.0	4320	3.2 ± 0.4	−127.0 ± 3.4	−103.6 ± 3.3
4343.4985	7.05 ± 1.85	−61.7 ± 7.5	4343	3.1 ± 0.3	−111.8 ± 3.0	−102.2 ± 4.1
*4405.2629	6.48 ± 0.53	−117.0 ± 2.4	4406	1.2 ± 0.3	−120.7 ± 7.4	−103.6 ± 2.8
4627.4868	7.82 ± 0.55	−12.9 ± 2.0	4629	2.0 ± 0.5	−129.7 ± 6.5	−90.3 ± 3.4
4654.4839	8.61 ± 0.52	−147.8 ± 1.7	4653	1.4 ± 0.4	−109.0 ± 7.4	−104.4 ± 2.2
4794.6152	2.60 ± 0.07	−143.1 ± 0.7	4787	1.4 ± 0.5	−155.3 ± 9.5	−123.2 ± 3.0
*4828.6533	0.79 ± 0.16	−155.4 ± 4.1	4822	2.5 ± 0.3	−162.0 ± 3.9	−112.6 ± 2.5

Notes. Columns: (1) epoch of optical observation; (2) optical degree of polarization; (3) optical position angle (P.A.) of polarization; (4) epoch of VLBA observation; (5) degree of polarization in the core region at 43 GHz; (6) P.A. of polarization in the core region at 43 GHz; (7) direction of the inner jet in projection on the sky plane.
[a] Symbol "*" marks epoch at which the optical polarization P.A. and EVPA in the 43 GHz core align within 1σ uncertainty.
[b] P.A.s of polarization at 43 GHz are corrected for RM according to Jorstad et al. (2007).

Table 7
Quasi-simultaneous Optical and 86 GHz Polarization Measurements

Epoch^{a}_{opt} (RJD) (1)	p_{opt} (%) (2)	φ_{opt} (deg) (3)	Epoch_{86} (RJD) (4)	p_{86} (%) (5)	φ_{86} (deg) (6)	Θ_{jet} (deg) (7)
4304.5098	13.84 ± 0.94	−82.1 ± 1.8	4304	2.61 ± 0.59	−110.4 ± 6.5	−86.9 ± 4.7
4313.4829	6.18 ± 0.83	−78.0 ± 3.9	4314	6.93 ± 1.19	−112.2 ± 4.9	−103.6 ± 3.3
*4342.4062	3.70 ± 1.31	−110.9 ± 10.1	4339	4.09 ± 0.54	−103.4 ± 3.8	−102.2 ± 4.1
4346.4395	9.35 ± 1.37	−28.4 ± 4.2	4346	3.62 ± 0.57	−105.9 ± 4.5	−102.2 ± 4.1
4355.4492	3.57 ± 1.93	−3.5 ± 9.7	4353	2.80 ± 0.47	−96.8 ± 4.8	−102.2 ± 4.1
4359.4316	12.91 ± 3.87	−41.9 ± 6.6	4357	2.11 ± 0.57	−100.0 ± 7.7	−103.5 ± 2.0
4371.3677	26.98 ± 1.89	−51.6 ± 2.0	4372	1.86 ± 0.56	−91.5 ± 8.6	−103.5 ± 2.0
4395.3691	23.48 ± 4.11	−169.1 ± 5.0	4393	1.45 ± 0.46	−102.4 ± 9.2	−103.6 ± 2.8
*4410.3267	14.09 ± 1.01	−99.5 ± 2.1	4408	1.46 ± 0.47	−87.3 ± 9.2	−103.6 ± 2.8
4768.4941	8.26 ± 1.72	−61.0 ± 8.6	4768	1.39 ± 1.02	−7.9 ± 21.1	−132.2 ± 3.5
4769.5107	4.11 ± 0.60	−58.0 ± 6.0	4769	1.79 ± 0.47	−169.6 ± 7.5	−132.2 ± 3.5
4773.7139	5.20 ± 1.42	−79.4 ± 7.8	4773	1.46 ± 0.47	−167.1 ± 9.1	−132.2 ± 3.5

Notes. Columns: (1) epoch of optical observation; (2) optical degree of polarization; (3) optical position angle (P.A.) of polarization; (4) epoch of observation at 86 GHz; (5) degree of polarization at 86 GHz; (6) P.A. of polarization at 86 GHz; (7) direction of the inner jet in projection on the sky plane.
[a] Symbol "*" marks epoch at which the optical polarization P.A. and EVPA at 86 GHz align within 1σ uncertainty.

independent, Bayes theorem yields a probability of $<3 \times 10^{-8}$ that the number of observed alignments between the optical and 43 GHz polarization P.A.s occurs by chance. This implies that the polarized emission at different wavelengths is governed by common properties or processes rather than by chance, in agreement with previous findings (Gabuzda et al. 2006; Jorstad et al. 2007; D'Arcangelo et al. 2007).

9.1. Rotation of Position Angle of Optical Polarization

Analysis of the optical polarization behavior during optical outbursts shows that each ejection coincides with a rotation of the optical polarization P.A. (Figure 22). The rotations have similar rates for events $K1$ and $K2$, $v^{K1}_{rot} = 8.7 \pm 1.1$ and $v^{K2}_{rot} = 7.7 \pm 0.8$ deg per day, while the rotation during the ejection of $K3$ is slower, $v^{K3}_{rot} = 5.2 \pm 0.7$ deg per day. We interpret this as evidence that the rotation of φ_{opt} originates in the acceleration and collimation zone (ACZ). We can rule out a stochastic rotation of the P.A. due to plasma turbulence (Marscher et al. 2008, 2010), given that all three events have the same sense of rotation and coincide with optical flares. In the ACZ, Poynting flux is converted to bulk kinetic energy through the Lorentz force, which rotates the magnetohydrodynamic (MHD) outflows and forms helical trajectories of disturbances propagating down the jet (Vlahakis & Königl 2004;

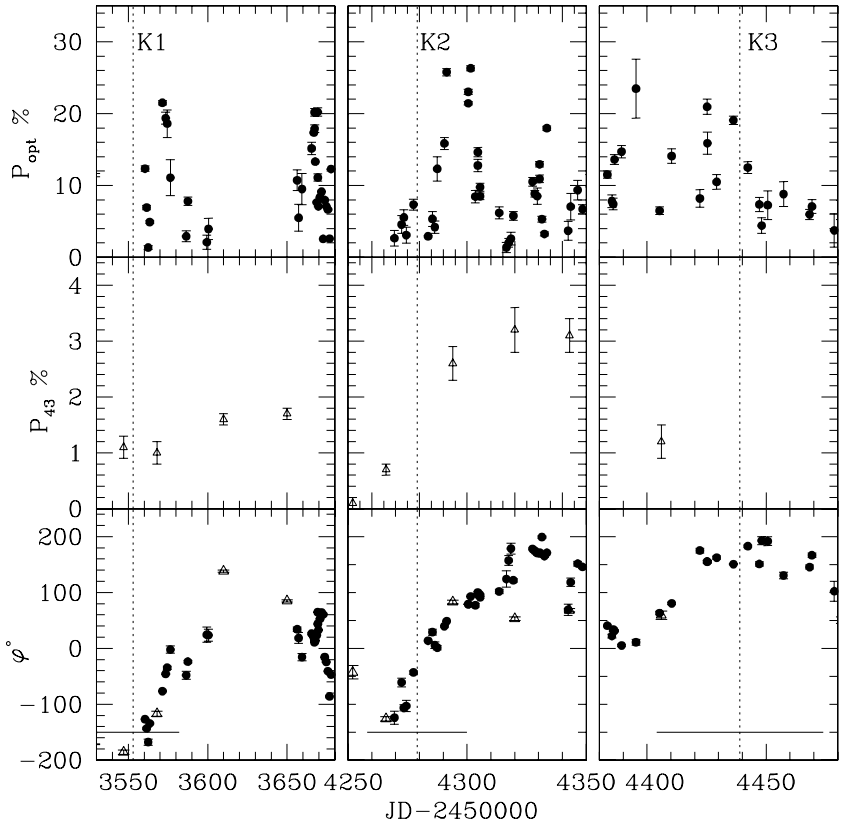

Figure 22. Polarimetric behavior at optical wavelengths (filled circles) and in 43 GHz core (open triangles) near the time of ejection of superluminal components (dotted lines), solid line segments show uncertainties in the ejection times.

Vlahakis 2006; Komissarov et al. 2007). The Lorentz factor should increase linearly with cross-sectional radius r, while the speed of rotation should decrease as r^{-1} to conserve angular momentum (Vlahakis 2006). If the polarized optical emission is produced in the ACZ by an emission feature that follows streamlines that execute a spiral path about the axis, then the speed of rotation of different disturbances should be inversely proportional to the final bulk Lorentz factor. The jet flow must travel farther from the BH to attain a higher Lorentz factor, hence the size scales of the site of EVPA rotation should be larger and the position of the core should shift downstream relative to states with a lower terminal Lorentz factor. In support of these predictions, the lowest rate of rotation is observed during event $K3$, which corresponds to the highest value of Γ, while $v_{\rm rot}^{\rm K1} \sim v_{\rm rot}^{\rm K2}$, in agreement with $\Gamma_{K1} \sim \Gamma_{K2}$ (see Table 1). Furthermore, there is a discontinuity in the motion of knot $K2$ near the time of ejection of $K3$ (see Figure 7), which could be explained if the 43 GHz core shifted downstream at this time. At the end of the optical EVPA rotation in events $K2$ and $K3$, the EVPA became chaotic, with average value perpendicular to the jet (see Figure 22). This is consistent with an optical outburst arising from an interaction between a disturbance propagating through a turbulent section in the jet and a standing shock system in the millimeter-wave core (D'Arcangelo et al. 2007).

Rotation of the optical EVPA associated with a disturbance propagating down the jet has been observed previously in BL Lacertae (Marscher et al. 2008) and in the quasars 3C 279 and PKS 1510−089 (Larionov et al. 2008; Marscher et al. 2010). There are several other properties of such rotations that are similar in BL Lac, 3C 279, PKS 1510−089, and 3C 454.3: (1) at the beginning of the rotation, the degree of polarization is low (∼1%–2%); (2) maximum fractional polarization is achieved when the E-vector aligns with the jet direction (for event $K1$, $P_{\rm max} = 22\%$, $\varphi_{\rm max} = -77^\circ$; for $K2$, $P_{\rm max} = 26\%$, $\varphi_{\rm max} = -87^\circ$; event $K3$ is undersampled); and (3) at the end of the rotation, the degree of polarization decreases. We infer that a rotation of the optical polarization P.A. during a prominent optical outburst is a common feature of blazars. In addition, in 3C 279 both the optical and 43 GHz core EVPAs rotate as a superluminal knot emerges from the core (Larionov et al. 2008). A few measurements of the EVPA in the core of 3C 454.3, simultaneous with optical polarization observations, agree with the optical EVPAs (Figure 22). However, the agreement occurs when $\varphi_{\rm opt}$ and φ_{43} are closely aligned with the jet direction (Table 6), so that it is possible that the core EVPA remains near that preferred angle instead of rotating with $\varphi_{\rm opt}$.

Despite agreement between $\varphi_{\rm opt}$ and φ_{43} for a number of essentially simultaneous observations (see Table 6), the majority of the high optical polarization measurements occur when the optical EVPA is perpendicular to the jet, while at 86 GHz and in the 43 GHz core, the majority of the E-vectors at high degrees of polarization lie along the jet direction. There are multiple possible reasons for this discrepancy: (1) high millimeter-wave polarization does not exceed 7%, while the optical degree of polarization $\geqslant$20% quite often; this is qualitatively consistent with the millimeter-wave polarization being affected by synchrotron self-absorption, which lowers the degree of polarization and rotates the EVPA by 90°; (2) the magnetic field in the core region has a helical structure, with the optical and millimeter-wave emission regions located in different parts of the helix; and (3) the jet has a spine-and-sheath structure such that, in a quiescent state, the optical polarization comes from a

transition zone between the fast spine stream and slower sheath flow (such emission would be highly polarized perpendicular to the outflow; Laing 1980; D'Arcangelo et al. 2009), while the millimeter-wave emission region is dominated by turbulence and has low polarization. In an active state, a disturbance in the jet defines the optical and millimeter-wave polarization properties: at millimeter wavelengths the disturbance orders the magnetic field perpendicular to the jet flow, while $\varphi_{\rm opt}$ depends on whether the disturbance or shear layer dominates the polarized flux.

10. DISCUSSION

We have found a connection between millimeter-wave and optical outbursts and disturbances propagating down the radio jet in 3C 454.3. At least three major optical outbursts, O_{K1}, O_{K2}, and O_{K3}, observed in 2005–2008 are related to superluminal knots identified in the VLBA images. Jorstad et al. (2007) have found that in blazars the polarization properties of superluminal knots at 43 GHz are consistent with weak shocks and the optical polarized emission originates in shocks, most likely situated between the 86 GHz and 43 GHz VLBI cores. It appears that shocks and their interaction with underlying jet structure might be generally responsible for optical and high-energy outbursts.

10.1. Location of the Optical Emission in the Jet

Comparison of the timing of optical outbursts and epochs of ejection of superluminal knots from the core can be used to determine the location of the sites where kinetic and internal energy is dissipated in the form of radiation. The delay between the peak of an outburst and the time of the ejection of the associated superluminal component, along with the apparent speed of the knot, determines the location of the optical outburst in the jet with respect to the core, $\Delta r_{\rm opt} = \beta_{\rm app} c \Delta T_{\rm opt} / \sin\Theta_{\circ}$. According to Tables 1 and 4, the peaks of outbursts O_{K1}, O_{K2}, and O_{K3} occurred 12.6 ± 5.6 pc upstream, 3.5 ± 3.7 pc downstream, and 2 ± 18 pc upstream of the core, respectively. The average location for O_{K2} and O_{K3} is 2.8 ± 3.4 pc downstream of the core. In the case of a conical structure of the jet, Jorstad et al. (2005) have estimated the half opening angle of the jet in 3C 454.3 to be $\theta = 0.^{\circ}8 \pm 0.^{\circ}2$. We have obtained an average size of the core during our period of observations using modeling by circular Gaussians, $a_{\rm core} = 0.068 \pm 0.011$ mas. This value of $a_{\rm core}$ gives an upper limit for the transverse size of the core, which, along with the opening angle of the jet, provides an estimate of the distance of the millimeter-wave core from the central engine, $R_{\rm BH} \leqslant 18 \pm 3$ pc. Therefore, if the perturbation that created $K1$ is responsible for O_{K1}, then the maximum of the outburst took place when $K1$ was located at a distance 5.4 ± 5.2 pc from the central engine, while the maxima of O_{K2} and O_{K3} outbursts occurred at a larger distance from the BH, 21 ± 4 pc, perhaps when knots $K2$ and $K3$ passed through the millimeter-wave core. This implies that the dissipation site for O_{K1} was closer to the central engine (BH) than that for outbursts O_{K2} and O_{K3}. These results are consistent with the recently advanced ideas that the dissipation sites of optical and high-energy outbursts can occur at different locations and involve different sources of seed photons (Ghisellini et al. 2007; Marscher et al. 2008, 2010; Chatterjee et al. 2008).

10.2. The Structure of the Millimeter-wave Core

The most powerful optical outburst, O_{K1}, preceded the passage of $K1$ through the 43 GHz core (ejection) by ∼50 days.

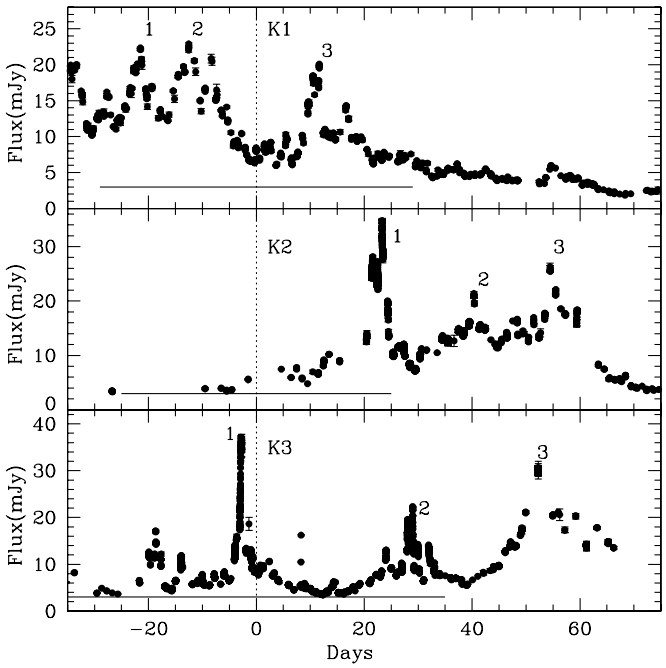

Figure 23. Optical photometric variability within $-1\sigma T_{\circ}$ to $+2\sigma T_{\circ}$ time interval relative to the time of the ejection, $T_{\circ}$ of each superluminal component (dotted line); values of $T_{\circ}$ and their uncertainties are given in Table 1.

In addition, there are optical flares (RJD: 3537 and RJD: 3561, see Table 3) that occurred within 1σ uncertainty of the time of ejection of $K1$. Outbursts O_{K2} and O_{K3} were simultaneous (within 1σ uncertainty) with the passage of $K2$ and $K3$, respectively, through the core. We isolate segments of the optical light curve within the time interval $-\sigma T_{\circ}$ and $+2\sigma T_{\circ}$ of each of knots $K1$, $K2$, and $K3$ (Figure 23, the values of $\sigma T_{\circ}$ are given in Table 1). Each ejection is accompanied by a series of flares (denoted in Figure 23 as 1, 2, and 3) that starts within 1σ of $T_{\circ}$. The duration of the series (time between the first and third peaks) is comparable, 50, 50, and 65 days, for events $K1$, $K2$, and $K3$, respectively.

The profile of event O_{K1} is very different from the profiles of O_{K2} and O_{K3}. The average of the rise and decay times for O_{K1} has a width of ∼47 days (Table 3), with a rise time of 68 days and a decay of only 26 days. Outbursts O_{K2} and O_{K3}, as well as the flares connected with the passage of $K1$ through the core, have much shorter durations and similar rise and decay times (see Figure 23). A possible interpretation is that, in the case of O_{K1}, located deeply within the ACZ, the energization of relativistic electrons is gradual and continuous, while for outbursts occurring in the VLBI core, relativistic electrons are energized abruptly owing to interaction between the disturbance and the core. The latter implies that the three-flare structure of optical outbursts seen in Figure 23 is related to the physical structure of the millimeter-wave core. Indeed, the super-resolved images of 3C 454.3 (Figure 6) support the idea that the core at 43 GHz might have a three-component structure.

The core might be a system of alternating conical shocks and rarefactions, as suggested by Gómez et al. (1997), Marscher (2006), and Cawthorne (2006). In this case, the distance between constrictions, $z_{\rm max}$, can be calculated for an ultra-relativistic equation of state according to Daly & Marscher (1988): $z_{\rm max} \approx 3.3 \times \Gamma a^{\rm t}_{\rm core}/\eta$, where $a^{\rm t}_{\rm core}$ is the transverse radius of the core in mas and $\eta = p_{\rm ext}/p_{\circ,\rm jet}$ is the ratio of the external pressure to initial pressure (i.e., at the upstream boundary of the core) in

Table 8
Longitudinal Size of the VLBI Core

Knot	$z_{\max}$ (mas)	$a_{\rm core}^{\ell,\rm theor}$ (mas)	$\Delta T_{\rm s}$ (days)	$a_{\rm core}^{\ell,\rm obs}$ (mas)
(1)	(2)	(3)	(4)	(5)
K1	0.50	0.026	50	0.013
K2	0.56	0.041	50	0.025
K3	1.01	0.011	65	0.018

Notes. Columns: (1) name of event; (2) distance between constrictions; (3) estimate of longitudinal size of the core from the theoretical model; (4) duration of series of outbursts; (5) estimate of longitudinal size of the core from observational consideration.

the jet. Jorstad et al. (2005) have found that the relation between the viewing angle and Lorentz factor in blazars is consistent with $\eta \sim 3$. If the core of 3C 454.3 is a system of three conical shocks, then the longitudinal size of the core in projection on the sky can be determined as $a_{\rm core}^{\ell,\rm theor} = 3 z_{\max} \sin\Theta_{\circ}$. On the other hand, if the three-flare structure of the optical outbursts observed in the vicinity of the ejection is caused by a disturbance moving through this system of conical shocks, then $a_{\rm core}^{\ell,\rm obs} = \Delta T_{\rm s} \mu$, where $\Delta T_{\rm s}$ is the duration of the optical outbursts and μ is the proper motion of the knot. Table 8 lists values of $a_{\rm core}^{\ell,\rm theor}$ and $a_{\rm core}^{\ell,\rm obs}$ for events $K1$, $K2$, and $K3$, which are consistent with the proposed association between a propagating disturbance and with the multi-component structure of the VLBI core providing a viable explanation for the three-flare pattern observed in the optical light curve. From standard gas dynamics, the presence of multiple standing shocks in three dimensions requires a high level of azimuthal symmetry of the pressure at the boundary of the jet in order for the structure to remain intact.

10.3. Location of Millimeter-wave Outbursts in the Jet

We have derived the locations of 230 GHz outbursts M_{K1}, M_{K2}, and M_{K3} in the same manner as for optical outbursts O_{K1}, O_{K2}, and O_{K3} owing their association with superluminal knots. The maxima of M_{K1}, M_{K2}, and M_{K3} occurred when a disturbance was located 4.6 ± 6.1 pc upstream, 8.2 ± 4.8 pc downstream, and 15 ± 37 pc downstream of the core, respectively, with the average value 3.8 ± 4.5 pc downstream of the 43 GHz core. This implies that the passage of a disturbance through the 230 GHz core should occur during the rising branch of a millimeter-wave outburst.

The sharp millimeter-wave outbursts $M1$ and $M2$ (see Figure 1) seem unrelated to the appearance of new knots although we cannot reject the possibility that new knots were ejected near the time of $M1$ and $M2$ but could not be resolved on the images because they were weaker than knots $K1$ and $K3$, which were ejected before outbursts $M1$ and $M2$, respectively. However, the VLBA observations support the idea that the outbursts are caused by curvature in the inner jet that decreases the angle between a disturbance ($K1$ or $K3$) and the line of sight so that the flux peaks when the disturbance passes through the minimum viewing angle, as suggested by Villata et al. (2007). Indeed, Figure 9 shows curvature in the trajectories of $K1$ and $K3$ at a distance ~0.05–0.07 mas from the core. This is the location of knots $K1$ and $K3$ when outbursts $M1$ and $M2$ peaked. Comparison of Tables 1 and 3 indicates that $M1$ peaked at a time close to the maximum flux of knot $K1$, and that the maximum of $M2$ occurred when knot $K3$ had the highest flux. The millimeter-wave spectral index during outbursts $M1$ and $M2$ corresponds to optically thin emission (see Section 8), as expected for radiation coming from downstream of the core. In addition, Table 3 shows that the timescale of $M1$ is ~4–5 times shorter than $w_{\rm mm}$ of $M2$, consistent with $K1$ moving closer to the jet axis (a smaller radius of curvature) and $K3$ moving along periphery of the jet (a larger radius of curvature), which agrees with the viewing angles of the knots (Table 1). We use the delay between the times of ejection of $K1$ and peak of $M1$, along with the kinematic parameters of $K1$, to derive the location of the curvature of the jet, which is 54 ± 16 pc downstream the core.

10.4. Location of the High-energy Emission in the Jet

The analysis of spectral characteristics of outbursts in 3C 454.3 reveals that neither during outbursts nor in quiescent states is the X-ray emission a continuation of the optical synchrotron spectrum. The most likely mechanism of X-ray production is inverse Compton scattering of low-energy photons by relativistic electrons, as suggested by Sikora et al. (2008) and Raiteri et al. (2008a).

Figure 2 displays normalized high-energy light curves, with the optical light curve superposed, during outburst O_{K1}, the period covering O_{K2} plus O_{K3}, and $M2$. Table 2 indicates that the strongest correlation between optical and X-ray variations was during O_{K1}, with a delay $\lesssim$1 day. Inspection of Figure 2 reveals that this correlation was dominated by the first ~15 days of the decaying branch of the outburst. (Unfortunately, the rising branch was not observed at X-rays and has a seasonal gap at optical frequencies; see Figure 1). According to the discussion above, the optical outburst took place upstream of the 43 GHz core. The X-ray outburst could have been produced via the EC mechanism, with the seed photons coming from the dusty torus, as argued by Sikora et al. (2008). Similarity in the decay at optical and X-ray frequencies implies that the primary cause of the outburst was an increase in the number of relativistic electrons. However, the EC model predicts that the X-ray spectrum should be rather flat (Ghisellini et al. 2007), whereas $\alpha_{\rm X}$ is steepest during O_{K1} (Table 5). Although this is comfortably less than $\alpha_{\rm opt}$, it is striking that the X-ray spectrum was flatter during the quiescent state. This can be understood if the X-ray emission during the quiescent state is dominated by the EC process while the SSC mechanism contributes significantly in the X-ray production during O_{K1}. A possible delay of X-ray variations by ~1 day relative to optical variations (Table 2) supports such a hypothesis (McHardy et al. 1999).

We have suggested that the optical flares observed within 1σ uncertainty of the time of ejection of $K1$ (Figure 23) originated in the VLBI core as the result of compression of the disturbance by standing shocks in the core. Figure 2 shows that two X-ray flares (designated as $X1$ and $X2$) occurred during the same time span, which implies that these X-ray flares originated in the millimeter-wave core as well, probably via the SSC mechanism. The SSC model is supported by tentative delays of several days relative to the optical peaks for flares $X1$ and $X2$, as can be inferred from Figure 2. The higher amplitude of the X-ray flares relative to the synchrotron flares (cf. Figure 2) is also expected in the SSC case if an increase in the number of relativistic electrons causes the events (Chatterjee et al. 2008).

The measurements during the O_{K2}+O_{K3} period (middle panel of Figure 2) show an increase in X-ray activity during O_{K2} and possibly O_{K3}. Vercellone et al. (2009) have found a good correlation between γ-ray and optical variations at the beginning of O_{K3}, and argue that the γ-ray emission is dominated by EC scattering of photons from the broad-line region by relativistic electrons in the jet. Although we agree that EC is probably

the dominant mechanism for γ-ray production, we argue that the optical outburst O_{K3} appears related to the 43 GHz core located ∼20 pc from the broad-line region. We propose that seed photons for the γ-ray production are local to the millimeter-VLBI core, arising from a slower sheath surrounding the spine, although synchrotron radiation from the disturbance itself plus the millimeter-wave core should contribute to the production of γ-rays as well (Marscher et al. 2010). The presence of such a sheath is supported by the wide range of apparent speeds observed in the jet, from 0.12 to 0.53 mas yr^{-1}(Jorstad et al. 2005).

The prominent millimeter-wave outburst $M2$ (see Figure 1) featured moderate γ-ray, X-ray, and optical flares. This high-frequency activity was especially pronounced during the early portion of the millimeter-wave outburst, but tapered off during its later stages. It is possible that a new superluminal knot was ejected during outburst $M2$, but could not be separated from $K3$ on the VLBA images. In this case, the multiple peaks of similar amplitude at 230 GHz, as well as the secondary optical maxima, can be explained by a knot passing through several standing shocks in the core region, as occurred during the passage of $K1$, $K2$, and $K3$ (Figure 23). In the absence of a new ejection, the millimeter-wave outburst is probably not associated with the optical variability, rather it is caused by a change of the viewing angle of $K3$ when the knot was ∼50 pc from the core (see Section 10.3). The optical emission could originate in the core according to polarization measurements, in a similar manner as proposed for the quasar 0420-014 (D'Arcangelo et al. 2007).

The γ-ray light curve during event $M2$ (bottom panel of Figure 2) is well correlated with the variations in optical flux, and the X-ray variations correlate with both the optical and γ-ray light curves, albeit less strongly. The γ-ray and optical variations were simultaneous within a day (Table 2), while the X-ray variations preceded the optical variations by 3 ± 2 days, although the X-ray measurements are sparse. The value of the X-ray spectral index during $M2$ is similar to α_X during O_{K1}. We suggest that the X-ray emission during $M2$ was produced via the SSC mechanism by the scattering of a wide spectrum of synchrotron photons—from far-IR to optical frequencies—by relativistic electrons with Lorentz factors $\gamma \sim 10^2$–10^3. This can explain the moderate correlation between the X-ray and optical variations and smoother X-ray variability. If the delay of the optical with respect to the X-ray variations is real, it can be understood in the manner proposed for the quasar 3C 279 (Chatterjee et al. 2008), in which relativistic electrons are accelerated gradually. In this case, the acceleration mechanism should be different from that for O_{K2} and O_{K3}, and probably involves turbulence in the core. This is consistent with a significantly lower degree of polarization in the 43 GHz relative to optical polarization if the two emission regions are co-spatial but occupy different volumes (Table 6).

Our analysis of the γ-ray and optical light curves confirms a strong correlation between the two wavelengths found by Bonning et al. (2009). The correlation persists beyond $M2$, with γ-ray and optical variations having similar amplitudes of variability (see Figure 2). Bonning et al. (2009) have concluded that the γ-ray outburst during $M2$ was dominated by EC scattering of IR/optical photons from the accretion disk and/or broad-line region by electrons with $\gamma \sim 10^3$–10^4. Although this may seem a reasonable explanation for the observed strong correlation between γ-ray and optical variations, polarization observations (see Figure 3 and Table 6) indicate that during $M2$ (RJD: 4550–4840) the P.A. of the optical polarization tended to align with φ_{43} in the core. This implies that the variable optical emission arose in the vicinity of the core, as discussed above. For this reason, we favor the alternative scenario, wherein the γ-rays are produced by scattering of synchrotron seed photons from the sheath of the jet.

We can be more specific regarding the nature of the seed photons by considering the steepening of the γ-ray spectrum above 2 GeV reported by Abdo et al. (2009b), from a spectral index of 1.3–2.5, along with steepening of the spectral index of synchrotron emission from 1.4 at near-IR to 2.3 at soft UV wavelengths (Table 5). We can explain the steepening of the γ-ray spectrum, as well as the rapid fall-off in the synchrotron emission toward higher ultraviolet frequencies by a steepening of the electron energy distribution above an energy $\gamma \sim 10^4$ in rest-mass units, where we assume a magnetic field strength $\lesssim$1 G. Recent theoretical calculations by Reynolds (2009) show that, for an inhomogeneous source, more pronounced steepening than by 0.5 in the source's integrated spectral index is possible due to a combination of synchrotron losses and geometrical effects. If the 2 GeV γ-rays are produced by the EC process, the seed photons should have observed frequencies near $10^{12}(\Gamma/25)^{-2}(\delta/25)^{-2}$ Hz. This favors either the putative dust torus (Sikora et al. 2008) or sheath of the jet as the source of the seed photons. The similarity of the γ-ray and optical light curves, including very rapid variations (see Section 7), can then be explained as a consequence of the variations being caused by changes in the number of electrons with $\gamma \sim 3 \times 10^3$–$10^4$ over a limited volume within a given disturbance.

11. CONCLUSIONS

The optical, X-ray, and radio light curves of blazars that have been assembled and analyzed over the past several years (e.g., Villata et al. 2004, 2009; Bach et al. 2006; Raiteri et al. 2008a; Chatterjee et al. 2008; Marscher et al. 2010) strongly support the conclusion that the long-term variability at all wavelengths is governed by physical activity in the relativistic jet that we can image with the VLBA. Our multifrequency study of the quasar 3C 454.3 during the dramatic activity of 2005–2008, including intense monitoring of the structure of the parsec-scale jet, reveals strong connections among the observed optical, X-ray, and γ-ray outbursts, its spectral and polarization behavior, and disturbances propagating down the jet.

We have found that the location of the most prominent X-ray and optical outburst (in 2005) was within ∼10 pc from the BH. The event was the result of a disturbance propagating down the jet through a photon field that included synchrotron radiation from both the high-Γ spine and slower sheath of the jet, and perhaps a hot dust torus (Sikora et al. 2008) with X-ray emission produced by both the SSC and EC mechanisms.

Our intensive monitoring with the VLBA at 43 GHz reveals that interaction between disturbances in the jet and the millimeter-wave core results in X-ray and optical outbursts and can cause optical intraday variability. This implies that the millimeter-wave core is a physical feature of the jet, e.g., a standing shock (Cawthorne 2006; Jorstad et al. 2007; D'Arcangelo et al. 2007), that is different from the cm-wave core, the location of which is probably determined by the jet opacity.

We have observed three events when the passage of a superluminal knot through the core coincided with a series of optical outbursts and an increase in the X-ray emission. We infer that the structure of the optical outbursts reflects the fine-scale structure in the core, a scenario supported by super-resolved

VLBA images. The X-ray production in the core region can be dominated by either the EC or SSC mechanism, depending on the properties of the disturbance, as suggested by Katarzynski & Ghisellini (2007).

Vercellone et al. (2009) have reported a good correlation between γ-ray and optical variations in autumn 2007, which coincides with a series of optical outbursts that we relate to an event in the core. This suggests that γ-ray emission is also produced during interactions within the core. If the γ-rays originate via the EC mechanism, then the seed photons should be local to the 43 GHz core and could come from the sheath of the jet.

We have observed three episodes of rotation of the P.A. of optical polarization near the times of passage of superluminal components through the core. We interpret this as evidence that the millimeter-wave core of 3C 454.3 is located near the end of the ACZ of the jet flow, where the magnetic field has a toroidal structure (e.g., Vlahakis 2006). Our findings agree with other studies reporting such rotations related to disturbances in the jet (Marscher et al. 2008, 2010; Larionov et al. 2008; Abdo et al. 2010). This implies that rotation of the optical polarization P.A. is a common occurrence during the early stages of flares in blazars. In the case of 3C 454.3, we tentatively infer an inverse relationship between the Lorentz factor of the superluminal component and the rate of rotation of the optical EVPA, as expected if higher values of Γ are reached farther from the BH where the jet has expanded to a larger cross-sectional radius.

Our study of the γ-ray bright quasar 3C 454.3 demonstrates an obvious connection between events at different wavelengths, the complexity of their relationships, and the primary role of the parsec-scale jet in the generation of these observed events. The ability of the *Fermi* LAT to produce well-sampled γ-ray light curves for the first time, combined with the ultra-high-resolution imaging of the VLBA and flux and polarization curves at other wavebands, provides an unprecedented opportunity to locate the events within the most compact regions of the jets of blazars. This endeavor makes possible a deeper understanding of the dynamics of relativistic jets and physics of the radiative processes.

The authors thank the referee for very useful comments. The research at Boston University (BU) was funded in part by NASA Fermi Guest Investigator grants NNX08AV65G and NNX08AV61G, and through Astrophysical Data Analysis Program grant NNX08AJ64G, and by the National Science Foundation (NSF) through grant AST-0907893. The VLBA is an instrument of the National Radio Astronomy Observatory, a facility of the National Science Foundation operated under cooperative agreement by Associated Universities, Inc. The St. Petersburg State University team acknowledges support from RFBR grant 09-02-00092. The research at the IAA-CSIC is supported in part by the Spanish "Ministerio de Ciencia e Innovación" through grant AYA2007-67626-C03-03. The effort at Steward Observatory was funded in part by NASA through Fermi Guest Investigator grant NNX08AV65G. The Metsähovi team acknowledges support from the Academy of Finland. We are grateful to the IRAM Director for providing discretionary observing time at the 30 m telescope. The PRISM camera at Lowell Observatory was developed by K. Janes et al. at BU and Lowell Observatory, with funding from the NSF, BU, and Lowell Observatory. The Calar Alto Observatory is jointly operated by the Max-Planck-Institut für Astronomie and the Instituto de Astrofísica de Andalucía-CSIC. The Liverpool telescope is operated on the island of La Palma by Liverpool John Moores University in the Spanish Observatorio del Roque de los Muchachos of the Instituto de Astrofisica de Canarias, with funding from the UK Science and Technology Facilities Council. Partly based on data taken and assembled by the WEBT collaboration and stored in the WEBT archive at the Osservatorio Astronomico di Torino-INAF (http://www.oato.inaf.it/blazars/webt/). The Submillimeter Array is a joint project between the Smithsonian Astrophysical Observatory and the Academia Sinica Institute of Astronomy and Astrophysics, and is funded by the Smithsonian Institution and the Academia Sinica. The IRAM 30 m telescope is supported by INSU/CNRS (France), MPG (Germany), and IGN (Spain). We acknowledge the *Swift* team for providing the public archive of *Swift*-XRT data, and we acknowledge Fermi GI grant NNX09AU07G for supporting the public archive of processed data.

REFERENCES

Abdo, A. A., et al. 2009a, ApJS, 183, 46
Abdo, A. A., et al. 2009b, ApJ, 699, 817
Abdo, A. A., et al. 2010, Nature, 463, 919
Agudo, I., et al. 2006, A&A, 456, 117
Agudo, I., et al. 2010, ApJS, submitted (arXiv:0911.5523)
Bach, U., et al. 2006, A&A, 456, 105
Bonning, E. W., et al. 2009, ApJ, 697, L81
Cawthorne, T. V. 2006, MNRAS, 367, 851
Chatterjee, R., et al. 2008, ApJ, 689, 79
Daly, R. A., & Marscher, A. P. 1988, ApJ, 334, 539
D'Arcangelo, F. D., et al. 2007, ApJ, 659, L107
D'Arcangelo, F. D., et al. 2009, ApJ, 697, 985
Dermer, C. D., & Atoyan, A. M. 2002, ApJ, 568, L81
Edelson, R. A., & Krolik, J. H. 1988, ApJ, 333, 646
Elvis, M., Wilkes, B. J., & Lockman, F. J. 1989, AJ, 97, 777
Gabuzda, D. C., Rastorgueva, E. A., Smith, P. S., & O'Sullivan, S. P. 2006, MNRAS, 369, 1596
Ghisellini, G., Foschini, L., Tavecchio, F., & Pian, E. 2007, MNRAS, 382, L82
Gómez, J. L., Martí, J. M., Marscher, A. P., Ibáñez, J. M., & Alberdi, A. 1997, ApJ, 482, L33
Gómez, J. L., et al. 2002, VLBA Scientific Memo 30 (NRAO)
Gurwell, M. A., Peck, A. B., Hostler, S. R., Darrah, M. R., & Katz, C. A. 2007, in ASP Conf. Ser. 375, From Z-Machines to ALMA: (Sub)millimeter Spectroscopy of Galaxies, ed. A. J. Baker et al. (San Francisco, CA: ASP), 234
Hagen-Thorn, V. A. 1997, Astron. Lett., 23, 19
Hagen-Thorn, V. A., et al. 2009, Astron. Rep., 53, 510
Jahoda, K., et al. 2006, ApJS, 163, 401
Jorstad, S. G., et al. 2005, AJ, 130, 1418
Jorstad, S. G., et al. 2007, AJ, 134, 799
Katarzynski, K., & Ghisellini, G. 2007, A&A, 463, 529
Komissarov, S. S., Barkov, M. V., Vlahakis, N., & Königl, A. 2007, MNRAS, 380, 51
Laing, R. A. 1980, MNRAS, 193, 439
Larionov, V. M., et al. 2008, A&A, 492, 389
Marscher, A. P. 2006, in AIP Conf. Proc. 856, Relativistic Jets: The Common Physics of AGN, Microquasars, and Gamma Ray Bursts, ed. P. A. Hughes & J. N. Bregman (Melville, NY: AIP), 1
Marscher, A. P., et al. 2008, Nature, 452, 966
Marscher, A. P., et al. 2010, ApJ, 710, L126
McHardy, I. M., et al. 1999, MNRAS, 310, 571
Mead, A. R. G., et al. 1990, A&AS, 83, 183
Moderski, R., Sikora, M., Coppi, P., & Aharonian, F. 2005, MNRAS, 363, 954
Perryman, M. A. C., et al. 1997, A&A, 323, L49
Raiteri, C. M., et al. 2007, A&A, 473, 819
Raiteri, C. M., et al. 2008a, A&A, 491, 755
Raiteri, C. M., et al. 2008b, A&A, 485, L17
Reynolds, S. P. 2009, ApJ, 703, 662
Savolainen, T., Wiik, K., Valtaoja, E., Jorstad, S. G., & Marscher, A. P. 2002, A&A, 394, 851
Schmidt, G. D., Elston, R., & Lupie, O. L. 1992, AJ, 104, 1563

Shepherd, M. C. 1997, in ASP Conf. Ser. 125, Astronomical Data Analysis Software and Systems VI, ed. G. Hunt & H. E. Payne (San Francisco, CA: ASP), 77
Sikora, M., Moderski, R., & Madejski, G. M. 2008, ApJ, 675, 71
Smith, P. S., et al. 1988, ApJ, 326, 39
Teräsranta, H., et al. 1998, A&AS, 132, 305
Thum, C., Wiesemeyer, H., Paubert, G., Navarro, S., & Morris, D. 2008, PASP, 120, 777
Tosti, G., et al. 2008, ATel, 1628, 1
Valtaoja, E., Lätheenmäki, A., Teräsranta, H., & Lainela, M. 1999, ApJS, 120, 95
Vercellone, S., et al. 2008, ApJ, 676, L13
Vercellone, S., et al. 2009, ApJ, 690, 1018
Villata, M., et al. 2004, A&A, 424, 497
Villata, M., et al. 2006, A&A, 453, 817
Villata, M., et al. 2007, A&A, 464, L5
Villata, M., et al. 2009, A&A, 501, 455
Vlahakis, N. 2006, in ASP Conf. Ser. 350, Blazar Variability Workshop II: Entering the GLAST Era, ed. H. R. Miller et al. (San Francisco, CA: ASP), 169
Vlahakis, N., & Königl, A. 2004, ApJ, 605, 656
Wardle, J. F. C., & Kronberg, P. P. 1974, ApJ, 194, 249
White, R. J., & Peterson, B. M. 1994, PASP, 106, 879
Zapatero, O. M. R., et al. 2005, ApJ, 621, 445